THE SIXTH DATA RELEASE OF THE SLOAN DIGITAL SKY SURVEY

Jennifer K. Adelman-McCarthy,[1] Marcel A. Agüeros,[2,3] Sahar S. Allam,[1,4] Carlos Allende Prieto,[5] Kurt S.J. Anderson,[6,7]
Scott F. Anderson,[8] James Annis,[1] Neta A. Bahcall,[9] C. A. L. Bailer-Jones,[10] Ivan K. Baldry,[11,12] J. C. Barentine,[5]
Bruce A. Bassett,[13,14] Andrew C. Becker,[8] Timothy C. Beers,[15] Eric F. Bell,[10] Andreas A. Berlind,[16]
Mariangela Bernardi,[17] Michael R. Blanton,[16] John J. Bochanski,[8] William N. Boroski,[1] Jarle Brinchmann,[18]
J. Brinkmann,[6] Robert J. Brunner,[19] Tamás Budavári,[12] Samuel Carliles,[12] Michael A. Carr,[9]
Francisco J. Castander,[20] David Cinabro,[21] R. J. Cool,[22] Kevin R. Covey,[23] István Csabai,[24,12]
Carlos E. Cunha,[25,26] James R. A. Davenport,[8] Ben Dilday,[27,26] Mamoru Doi,[28] Daniel J. Eisenstein,[22]
Michael L. Evans,[8] Xiaohui Fan,[22] Douglas P. Finkbeiner,[23] Scott D. Friedman,[29] Joshua A. Frieman,[1,25,26]
Masataka Fukugita,[30] Boris T. Gänsicke,[31] Evalyn Gates,[25] Bruce Gillespie,[6] Karl Glazebrook,[32]
Jim Gray,[33] Eva K. Grebel,[34,35] James E. Gunn,[9] Vijay K. Gurbani,[1,36] Patrick B. Hall,[37]
Paul Harding,[38] Michael Harvanek,[39] Suzanne L. Hawley,[8] Jeffrey Hayes,[40] Timothy M. Heckman,[12]
John S. Hendry,[1] Robert B. Hindsley,[41] Christopher M. Hirata,[42] Craig J. Hogan,[8] David W. Hogg,[16]
Joseph B. Hyde,[17] Shin-ichi Ichikawa,[43] Željko Ivezić,[8] Sebastian Jester,[10] Jennifer A. Johnson,[44]
Anders M. Jorgensen,[45] Mario Jurić,[42] Stephen M. Kent,[1] R. Kessler,[46] S. J. Kleinman,[47]
G. R. Knapp,[9] Richard G. Kron,[25,1] Jurek Krzesinski,[6,48] Nikolay Kuropatkin,[1] Donald Q. Lamb,[25,46]
Hubert Lampeitl,[29] Svetlana Lebedeva,[1] Young Sun Lee,[15] R. French Leger,[1] Sébastien Lépine,[49]
Marcos Lima,[27,26] Huan Lin,[1] Daniel C. Long,[6] Craig P. Loomis,[9] Jon Loveday,[50]
Robert H. Lupton,[9] Olena Malanushenko,[6] Viktor Malanushenko,[6] Rachel Mandelbaum,[42,51]
Bruce Margon,[52] John P. Marriner,[1] David Martínez-Delgado,[53] Takahiko Matsubara,[54]
Peregrine M. McGehee,[55] Timothy A. McKay,[56] Avery Meiksin,[57] Heather L. Morrison,[38]
Jeffrey A. Munn,[58] Reiko Nakajima,[17] Eric H. Neilsen, Jr.,[1] Heidi Jo Newberg,[59]
Robert C. Nichol,[60] Tom Nicinski,[1,61] Maria Nieto-Santisteban,[12] Atsuko Nitta,[47]
Sadanori Okamura,[62] Russell Owen,[8] Hiroaki Oyaizu,[25,26] Nikhil Padmanabhan,[63,51]
Kaike Pan,[6] Changbom Park,[64] John Peoples, Jr.,[1] Jeffrey R. Pier,[58]
Adrian C. Pope,[65] Norbert Purger,[24] M. Jordan Raddick,[12] Paola Re Fiorentin,[10]
Gordon T. Richards,[66] Michael W. Richmond,[67] Adam G. Riess,[12]
Hans-Walter Rix,[10] Constance M. Rockosi,[68] Masao Sako,[17,69]
David J. Schlegel,[63] Donald P. Schneider,[70] Matthias R. Schreiber,[71]
Axel D. Schwope,[72] Uroš Seljak,[73,74] Branimir Sesar,[8] Erin Sheldon,[25,26]
Kazu Shimasaku,[62] Thirupathi Sivarani,[15] J. Allyn Smith,[75]
Stephanie A. Snedden,[6] Matthias Steinmetz,[72] Michael A. Strauss,[9]
Mark SubbaRao,[25,76] Yasushi Suto,[77] Alexander S. Szalay,[12]
István Szapudi,[65] Paula Szkody,[8] Max Tegmark,[78] Aniruddha R. Thakar,[12]
Christy A. Tremonti,[22] Douglas L. Tucker,[1] Alan Uomoto,[79]
Daniel E. Vanden Berk,[70] Jan VandenBerg,[12] S. Vidrih,[80]
Michael S. Vogeley,[66] Wolfgang Voges,[81] Nicole P. Vogt,[7]
Yogesh Wadadekar,[9] David H. Weinberg,[44]
Andrew A. West,[82] Simon D. M. White,[83] Brian C. Wilhite,[19,84]
Brian Yanny,[1] D. R. Yocum,[1] Donald G. York,[25,46]
Idit Zehavi,[38] and Daniel B. Zucker[80]

[1] Fermi National Accelerator Laboratory, P.O. Box 500, Batavia, IL 60510.
[2] Columbia Astrophysics Laboratory, 550 West 120th Street, New York, NY 10027.
[3] NSF Astronomy and Astrophysics Postdoctoral Fellow.
[4] Department of Physics and Astronomy, University of Wyoming, Laramie, WY 82071.
[5] McDonald Observatory and Department of Astronomy, The University of Texas, 1 University Station, C1400, Austin, TX 78712-0259.
[6] Apache Point Observatory, P.O. Box 59, Sunspot, NM 88349.
[7] Department of Astronomy, New Mexico State University, MSC 4500, P.O. Box 30001, Las Cruces, NM 88003.
[8] Department of Astronomy, University of Washington, Box 351580, Seattle, WA 98195.
[9] Department of Astrophysical Sciences, Princeton University, Princeton, NJ 08544.
[10] Max-Planck-Institut für Astronomie, Königstuhl 17, D-69117 Heidelberg, Germany.
[11] Astrophysics Research Institute, Liverpool John Moores University, Twelve Quays House, Egerton Wharf Birkenhead CH41 1LD, UK.
[12] Center for Astrophysical Sciences, Department of Physics and Astronomy, Johns Hopkins University, 3400 North Charles Street, Baltimore, MD 21218.

[13] South African Astronomical Observatory, Observatory, Cape Town, South Africa.
[14] University of Cape Town, Rondebosch, Cape Town, South Africa.
[15] Department of Physics and Astrophysics, Center for the Study of Cosmic Evolution (CSCE) , and Joint Institute for Nuclear Astrophysics (JINA), Michigan State University, East Lansing, MI 48824.
[16] Center for Cosmology and Particle Physics, Department of Physics, New York University, 4 Washington Place, New York, NY 10003.
[17] Department of Physics and Astronomy, University of Pennsylvania, 209 South 33rd Street, Philadelphia, PA 19104.
[18] Centro de Astrofísica da Universidade do Porto, Rua das Estrelas-4150-762 Porto, Portugal.
[19] Department of Astronomy, University of Illinois, 1002 West Green Street, Urbana, IL 61801.
[20] Institut de Ciències de l'Espai (IEEC/CSIC), Campus UAB, E-08193 Bellaterra, Barcelona, Spain.
[21] Department of Physics and Astronomy, Wayne State University, Detroit, MI 48202.
[22] Steward Observatory, 933 North Cherry Avenue, Tucson, AZ 85721.
[23] Harvard-Smithsonian Center for Astrophysics, 60 Garden Street, Cambridge MA 02138.

ABSTRACT

This paper describes the Sixth Data Release of the Sloan Digital Sky Survey. With this data release, the imaging of the northern Galactic cap is now complete. The survey contains images and parameters of roughly 287 million objects over 9583 deg^2, including scans over a large range of Galactic latitudes and longitudes. The survey also includes 1.27 million spectra of stars, galaxies, quasars, and blank sky (for sky subtraction) selected over 7425 deg^2. This release includes much more stellar spectroscopy than was available in previous data releases and also includes detailed estimates of stellar temperatures, gravities, and metallicities. The results of improved photometric calibration are now available, with uncertainties of roughly 1% in g, r, i, and z, and 2% in u, substantially better than the uncertainties in previous data releases. The spectra in this data release have improved wavelength and flux calibration, especially in the extreme blue and extreme red, leading to the qualitatively better determination of stellar types and radial velocities. The spectrophotometric fluxes are now tied to point-spread function magnitudes of stars rather than fiber magnitudes. This gives more robust results in the presence of seeing variations, but also implies a change in the spectrophotometric scale, which is now brighter by roughly 0.35 mag. Systematic errors in the velocity dispersions of galaxies have been fixed, and the results of two independent codes for determining spectral classifications and redshifts are made available. Additional spectral outputs are made available, including calibrated spectra from individual 15 minute exposures and the sky spectrum subtracted from each exposure. We also quantify a recently recognized

[24] Department of Physics of Complex Systems, Eötvös Loránd University, Pf. 32, H-1518 Budapest, Hungary.

[25] Department of Astronomy and Astrophysics, University of Chicago, 5640 South Ellis Avenue, Chicago, IL 60637.

[26] Kavli Institute for Cosmological Physics, University of Chicago, 5640 South Ellis Avenue, Chicago, IL 60637.

[27] Department of Physics, University of Chicago, 5640 South Ellis Avenue, Chicago, IL 60637.

[28] Institute of Astronomy, Graduate School of Science, The University of Tokyo, 2-21-1 Osawa, Mitaka, 181-0015, Japan.

[29] Space Telescope Science Institute, 3700 San Martin Drive, Baltimore, MD 21218.

[30] Institute for Cosmic Ray Research, The University of Tokyo, 5-1-5 Kashiwa, Kashiwa City, Chiba 277-8582, Japan.

[31] Department of Physics, University of Warwick, Coventry CV4 7AL, UK.

[32] Centre for Astrophysics and Supercomputing, Swinburne University of Technology, P.O. Box 218, Hawthorn, VIC 3122, Australia.

[33] Microsoft Research, 455 Market Street, Suite 1690, San Francisco, CA 94105.

[34] Astronomical Institute, Department of Physics and Astronomy, University of Basel, Venusstrasse 7, CH-4102 Binningen, Switzerland.

[35] Astronomisches Rechen-Institut, Zentrum für Astronomie, University of Heidelberg, Mönchhofstrasse 12-14, D-69120 Heidelberg, Germany.

[36] Bell Laboratories, Alcatel-Lucent, 2701 Lucent Lane, Rm. 9F-546, Lisle, IL 60532.

[37] Department of Physics and Astronomy, York University, 4700 Keele Street, Toronto, ON, M3J 1P3, Canada.

[38] Department of Astronomy, Case Western Reserve University, Cleveland, OH 44106.

[39] Lowell Observatory, 1400 West Mars Hill Road, Flagstaff, AZ 86001.

[40] Institute for Astronomy and Computational Sciences, Physics Department, Catholic University of America, Washington, DC 20064.

[41] Remote Sensing Division, Naval Research Laboratory, Code 7215, 4555 Overlook Avenue SW, Washington, DC 20392.

[42] Institute for Advanced Study, Einstein Drive, Princeton, NJ 08540.

[43] National Astronomical Observatory, 2-21-1 Osawa, Mitaka, Tokyo 181-8588, Japan.

[44] Department of Astronomy, Ohio State University, 140 West 18th Avenue, Columbus, OH 43210.

[45] Electrical Engineering Department, New Mexico Institute of Mining and Technology, 801 Leroy Place, Socorro, NM 87801.

[46] Enrico Fermi Institute, University of Chicago, 5640 South Ellis Avenue, Chicago, IL 60637.

[47] Gemini Observatory, 670 N. A'ohoku Place, Hilo, HI 96720.

[48] Obserwatorium Astronomiczne na Suhorze, Akademia Pedagogiczna w Krakowie, ulica Podchorążych 2, PL-30-084 Kracŏw, Poland.

[49] Department of Astrophysics, American Museum of Natural History, Central Park West at 79th Street, New York, NY 10024.

[50] Astronomy Centre, University of Sussex, Falmer, Brighton BN1 9QH, UK.

[51] Hubble Fellow.

[52] Department of Astronomy and Astrophysics, University of California, Santa Cruz, CA 95064.

[53] Instituto de Astrofisica de Canarias, La Laguna, Spain.

[54] Department of Physics and Astrophysics, Nagoya University, Chikusa, Nagoya 464-8602, Japan.

[55] IPAC, MS 220-6, California Institute of Technology, Pasadena, CA 91125.

[56] Department of Physics, University of Michigan, 500 East University Avenue, Ann Arbor, MI 48109.

[57] SUPA, Institute for Astronomy, Royal Observatory, University of Edinburgh, Blackford Hill, Edinburgh EH9 3HJ, UK.

[58] US Naval Observatory, Flagstaff Station, 10391 West Naval Observatory Road, Flagstaff, AZ 86001-8521.

[59] Department of Physics, Applied Physics, and Astronomy, Rensselaer Polytechnic Institute, 110 Eighth Street, Troy, NY 12180.

[60] Institute of Cosmology and Gravitation (ICG), Mercantile House, Hampshire Terrace, University of Portsmouth, Portsmouth, PO1 2EG, UK.

[61] CMC Electronics Aurora, 84 North Dugan Road, Sugar Grove, IL 60554.

[62] Department of Astronomy and Research Center for the Early Universe, Graduate School of Science, The University of Tokyo, 7-3-1 Hongo, Bunkyo, Tokyo 113-0033, Japan.

[63] Lawrence Berkeley National Laboratory, One Cyclotron Road, Berkeley, CA 94720.

[64] Korea Institute for Advanced Study, 207-43 Cheong-Nyang-Ni, 2 dong, Seoul 130-722, Korea.

[65] Institute for Astronomy, 2680 Woodlawn Road, Honolulu, HI 96822.

[66] Department of Physics, Drexel University, 3141 Chestnut Street, Philadelphia, PA 19104.

[67] Department of Physics, Rochester Institute of Technology, 84 Lomb Memorial Drive, Rochester, NY 14623-5603.

[68] UCO/Lick Observatory, University of California, Santa Cruz, CA 95064.

[69] Kavli Institute for Particle Astrophysics and Cosmology, Stanford University, P.O. Box 20450, MS29, Stanford, CA 94309.

[70] Department of Astronomy and Astrophysics, Pennsylvania State University, 525 Davey Laboratory, University Park, PA 16802.

[71] Universidad de Valparaiso, Departamento de Fisica y Astronomia, Valparaiso, Chile.

[72] Astrophysical Institute Potsdam, An der Sternwarte 16, 14482 Potsdam, Germany.

[73] Joseph Henry Laboratories, Princeton University, Princeton, NJ 08544.

[74] Institute for Theoretical Physics, University of Zurich, Zurich 8057, Switzerland.

[75] Department of Physics and Astronomy, Austin Peay State University, P.O. Box 4608, Clarksville, TN 37040.

[76] Adler Planetarium and Astronomy Museum, 1300 Lake Shore Drive, Chicago, IL 60605.

[77] Department of Physics and Research Center for the Early Universe, Graduate School of Science, The University of Tokyo, 7-3-1 Hongo, Bunkyo, Tokyo 113-0033, Japan.

[78] Department of Physics, Massachusetts Institute of Technology, Cambridge, MA 02139.

[79] Observatories of the Carnegie Institution of Washington, 813 Santa Barbara Street, Pasadena, CA 91101.

[80] Institute of Astronomy, University of Cambridge, Madingley Road, Cambridge CB3 0HA, UK.

[81] Max-Planck-Institut für extraterrestrische Physik, Giessenbachstrasse 1, D-85741 Garching, Germany.

[82] Astronomy Department, University of California, 601 Campbell Hall, Berkeley, CA 94720-3411.

[83] Max Planck Institut für Astrophysik, Postfach 1, D-85748 Garching, Germany.

[84] National Center for Supercomputing Applications, 1205 West Clark Street, Urbana, IL 61801.

underestimation of the brightnesses of galaxies of large angular extent due to poor sky subtraction; the bias can exceed 0.2 mag for galaxies brighter than $r = 14$ mag.

Subject headings: atlases — catalogs — surveys

Online material: color figures

1. INTRODUCTION

The Sloan Digital Sky Survey (SDSS; York et al. 2000) is a comprehensive imaging and spectroscopic survey of the optical sky using a dedicated 2.5 m telescope (Gunn et al. 2006) at Apache Point Observatory in southern New Mexico. The telescope has a $3°$ diameter field of view, and the imaging uses a drift-scanning camera (Gunn et al. 1998) with 30 2048×2048 CCDs at the focal plane which image the sky in five broad filters covering the range from 3000 to 10000 Å (Fukugita et al. 1996; Stoughton et al. 2002). The imaging is carried out on moonless and cloudless nights of good seeing (Hogg et al. 2001), and the resulting images are calibrated photometrically (Tucker et al. 2006; Padmanabhan et al. 2007) to a series of photometric standards around the sky (Smith et al. 2002). After astrometric calibration (Pier et al. 2003) the properties of detected objects in the five filters are measured in detail (Lupton et al. 2001; Stoughton et al. 2002). Subsets of these objects are selected for spectroscopy, including galaxies (Strauss et al. 2002; Eisenstein et al. 2001), quasars (Richards et al. 2002), and stars. The spectroscopic targets are assigned to a series of plates containing 640 objects each (Blanton et al. 2003), and spectra are measured using a pair of double spectrographs, each covering the wavelength range 3800–9200 Å with a resolution $\lambda/\Delta\lambda$ which varies from 1850 to 2200. These spectra are wavelength- and flux-calibrated, and classifications and redshifts, as well as spectral types for stars, are determined by a series of software pipelines (Subbarao et al. 2002). The data are then made available both through an object-oriented database (the Catalog Archive Server [CAS]) and as flat data files (the Data Archive Server [DAS]).

The SDSS telescope saw first light in 1998 May, and entered routine operations in 2000 April. We have issued a series of yearly public data releases, which have been described in accompanying papers (Stoughton et al. 2002, hereafter the Early Data Release [EDR] paper; Abazajian et al. 2003, 2004, 2005, hereafter the DR1, DR2, and DR3 papers, respectively; Adelman-McCarthy et al. 2006, 2007, hereafter the DR4 and DR5 papers, respectively). The current paper describes the Sixth Data Release (DR6), which includes data taken through 2006 June. Access to the data themselves may be found on the DR6 Web site.[85] This Web site includes links to both the CAS and DAS Web sites, which contain extensive documentation on how to access the data.

When the SDSS started routine operations, the budget funded operations for 5 years, i.e., through the summer of 2005. Additional funding from the National Science Foundation, the Alfred P. Sloan Foundation, and the member institutions secured another 3 years of operations, and the present data release includes data from the first year of this extended period, termed SDSS-II. SDSS-II has three components: Legacy, which aims to complete the imaging and spectroscopy of a contiguous $\sim$7700 deg^2 region in the northern Galactic cap, Sloan Extension for Galactic Understanding and Exploration (SEGUE), which is carrying out an additional 3500 deg^2 of imaging and spectroscopy of 240,000 stars to study the structure of our Milky Way, and Supernova (Frieman et al. 2007), which repeatedly images a $\sim$300 deg^2

[85] See http://www.sdss.org/dr6.

equatorial stripe in the southern Galactic cap to search for supernovae in the redshift range $0.05 < z < 0.35$ for measurement of the redshift-distance relation.

DR6 is cumulative, in the sense that it includes all data that were included in previous data releases. However, as we describe in detail in this paper, we have incorporated into this data release a number of improvements and additions to the software. These include the following.

1. Improved photometric calibration, using overlaps between the imaging scans.
2. Improved wavelength and flux calibration of the spectra.
3. Improved velocity dispersion measurements for galaxies.
4. Results of an independent determination of galaxy and quasar redshifts and stellar radial velocities.
5. Effective temperatures, surface gravities and metallicities for many stars with spectra.

All DR6 data, including those included in previous releases, have been reprocessed with the new software.

In § 2 the sky coverage of the data included in DR6 is presented. Section 3 describes new features of the imaging data, including extensive low-latitude imaging, target selection of the SEGUE plates, improved photometric calibration, and a recently recognized systematic error in sky subtraction which affects the photometry of bright galaxies. Section 4 describes the extensive reprocessing we have done of our spectra, including improved flux and wavelength calibration, the determination of surface temperatures, metallicities and gravities of stars with spectra, the availability of two independent determinations of object redshifts, and improved velocity dispersions of galaxies. We summarize DR6 in § 5.

2. THE SKY COVERAGE OF THE SDSS DR6

In the spring of 2006, the imaging for the SDSS Legacy survey was essentially completed. The northern Galactic cap in DR6 is now contiguous, with the exception of 10 deg^2 spread among several holes in the survey; these have since been imaged, and will be included in the Seventh Data Release. The northern Galactic cap imaging survey covers 7668 deg^2 in DR6; the additional Legacy scans in the southern Galactic cap bring the total to 8417 deg^2. The sky coverage of the imaging data is shown in Figure 1, and is tabulated in Table 1. The images, spectra, and resulting catalogs are all available from the DAS; with a few exceptions noted below, all the catalogs are available from the CAS as well.

The imaging data are the union of three data sets:

1. Legacy data, which includes the large contiguous region in the northern Galactic cap, as well as three $2.5°$ wide stripes in the southern Galactic cap. These are shown in gray in Figure 1. The lighter gray indicates those regions new to DR6, containing 417 deg^2; the entire Legacy area available in DR6 is 8417 deg^2.
2. Imaging stripes (also $2.5°$ wide) as part of the SEGUE survey. These do not aim to cover a contiguous area, but are separated by roughly $20°$ and are designed to sparsely sample the large-scale distribution of stars in the Galactic halo. These cover just under 1600 deg^2 and are all available in the DAS. Notice
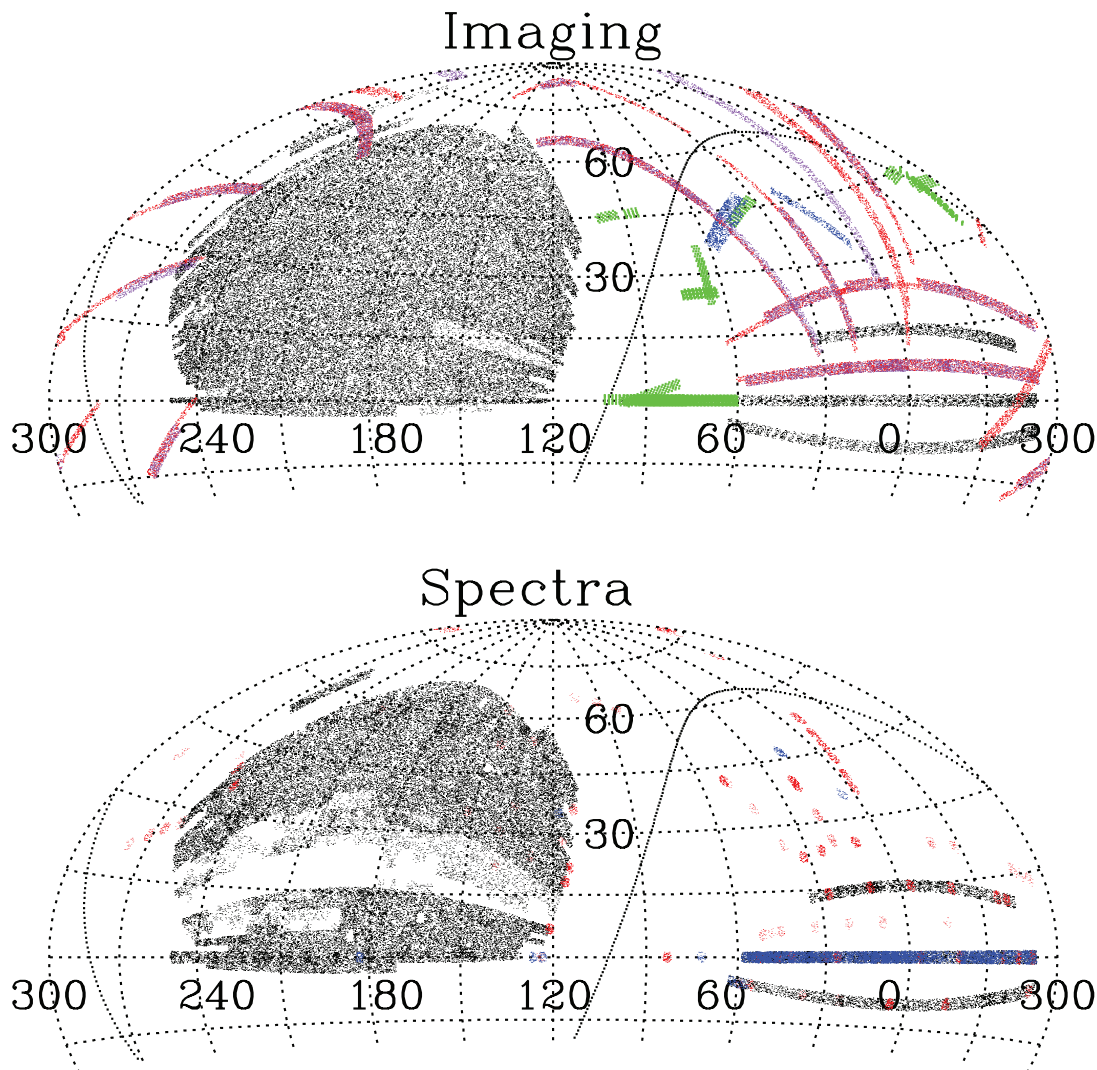
FIG. 1.—Distribution on the sky of the data included in DR6 (*top*: imaging; *bottom*: spectra), shown in an Aitoff equal-area projection in J2000.0 equatorial coordinates. The Galactic plane is the sinuous line that goes through each panel. The center of each panel is at $\alpha = 120° \equiv 8^h$, and that the plots cut off at $\delta = -20°$. The Legacy imaging survey covers the contiguous area of the northern Galactic cap (centered roughly at $\alpha = 200°$, $\delta = 30°$), as well as three stripes (each of width 2.5°) in the southern Galactic cap. The regions new to DR6 are shown in lighter shading than the rest in both panels. In addition, several stripes (blue in the imaging data) are auxiliary imaging data in the vicinity of M31 and the Perseus Cluster, while the SEGUE imaging scans are available in the DAS and CAS (*red*) and DAS only (*purple*). The green scans are additional runs as described in Finkbeiner et al. (2004). In the spectroscopy panel, special plates (in the sense of the DR4 paper) are indicated in blue, while SEGUE plates are in red. Note that many plates overlap; for example, there are SEGUE plates in the contiguous area of the northern Galactic cap, and the equatorial stripe in the southern Galactic cap, which appears solid blue, is also completely covered by the Legacy survey.

that many of these stripes go to quite low Galactic latitude, and some cross the Galactic plane. As we describe in § 3.1, the SDSS photometric pipeline is not optimized for crowded fields, and thus, the photometry of objects at the lowest Galactic latitudes is not reliable. Of these data, 1166 deg² are available in the CAS in a separate database from the Legacy imaging; these are the regions in which the outputs of the photometric pipeline are most reliable and which have been used for spectroscopic targeting (§ 3.2). The SEGUE imaging that is available in both CAS and DAS is indicated in Figure 1 in red; purple indicates the area only available in the DAS.

3. Additional imaging taken as part of various auxiliary programs as part of the SDSS, including scans of the region around M31 and Perseus (see the description in the DR5 paper), and adding up to roughly 26 deg². These scans are indicated in Figure 1 in blue. These data are not included in the CAS, but are available in the DAS.

In addition, the 2.5° wide equatorial stripe (stripe 82) in the southern Galactic cap has been imaged multiple times through the course of the SDSS, and again as part of the Supernova component of SDSS-II (Frieman et al. 2007). The 65 scans of stripe 82 observed through the fall of 2004 are of survey quality, i.e., they were taken under moonless and cloudless skies in good seeing. As in DR5, we make the calibrated object catalogs and the images corrected for bias, flat field, and image defects available through the DAS. There were an additional 171 supernova runs taken in the fall seasons of 2005 and 2006. Much of these data were taken under nonphotometric conditions, poor seeing, or during bright moon, and thus, the photometry is not reliable at face value (although Ivezić et al. [2007] have demonstrated that it can be calibrated quite well after the fact). The images and the uncalibrated object catalogs for these runs are made available through the DAS as well. Stripe 82 is composed of two overlapping strips (York et al. 2000), and Figure 2 shows the number

TABLE 1
Coverage and Contents of DR6

Parameter	Value
Imaging	
Imaging area in CAS	9583 deg^2
Imaging catalog in CAS	287 million unique objects
Legacy footprint area	8417 deg^2 (5% increment over DR5)
Legacy imaging catalog	230 million unique objects
SEGUE footprint area, available in DAS[a]	1592 deg^2
SEGUE footprint area, available in CAS	1166 deg^2
SEGUE imaging catalog	57 million unique objects
M31, Perseus scan area	~26 deg^2
Southern equatorial stripe with > 50 repeat scans	~300 deg^2
Commissioning ("Orion") data	832 deg^2
Spectroscopy	
Spectroscopic footprint area	7425 deg^2 (20% increment over DR5)
Legacy	6860 deg^2
SEGUE	565 deg^2
Total number of plate observations (640 fibers each)	1987
Legacy survey plates	1520
SEGUE plates	162
Special program plates	226
Repeat observations of plates	79
Total number of spectra	1,271,680
Galaxies[b]	790,860
Quasars	103,647
Stars	287,071
Sky	68,770
Unclassifiable	21,332
Spectra after removing skies and duplicates	1,115,971

[a] Includes regions of high stellar density, where the photometry is likely to be poor. See text for details.
[b] Spectral classifications from the `spectro1d` code; numbers include duplicates. The complete MAIN sample (Strauss et al. 2002) includes 585,719 galaxies after duplicates are removed, while the luminous red galaxy sample (Eisenstein et al. 2001) contains 79,891 galaxies.

of times each right ascension of the two strips is covered in the data through 2004 and as part of the Supernova survey.

Finkbeiner et al. (2004) made available 470 deg^2 of imaging on the southern equatorial stripe taken early in the survey but not included in either the DAS or the CAS. With DR6, we release an additional 362 deg^2 of imaging data; these runs are indicated in green in Figure 1.

The DR6 spectroscopy contains 1,271,680 spectra over 1987 plate observations. Of these, 1520 plates are from the main Legacy survey, and there are 64 repeat observations ("extra plates") of 55 distinct Legacy plates. In addition, there are 234 observations of 226 distinct "special" plates of the various programs described in the DR5 paper,[86] indicated in blue in Figure 1, and 169 observations of 162 distinct special plates taken as part of SEGUE (see § 3.2) (red in Fig. 1). In total, these plates cover 7425 deg^2 (not including overlaps). There are 32 fibers (64 fibers for the SEGUE plates) dedicated to background sky subtraction on each plate, about 0.7% of spectra are repeat observations on overlapping plates for quality assurance (and science; see e.g., Wilhite et al. 2005) and roughly 1% of spectra are too low in signal-to-noise ratio (S/N) for unambiguous classification, so there are roughly 1.1 million distinct objects with useful spectra in the DR6. This represents a roughly 20% increase over DR5. The areas of sky new to DR6 are represented in lighter gray in

[86] An updated special-plate list is available online at http://www.sdss.org/dr6/products/spectra/special.html.

Figure 1. We plan to complete the spectroscopy of the contiguous area of the northern Galactic cap in the spring of 2008.

The average seeing (see Fig. 4 of the DR1 paper) and limiting magnitude of the imaging data, as well as the typical S/N of the main survey spectra, are essentially unchanged from previous data releases; see the summary of survey characteristics in Table 1 of the DR5 paper.

3. CHARACTERIZATION AND USE OF THE IMAGING DATA

The SDSS photometric processing pipeline has been stable since DR2, and thus, the quantities measured for all objects included in DR5 have been copied wholesale into DR6. This version of the pipeline has been used for the small amount of northern Galactic cap data new to DR6, as well as the SEGUE imaging scans shown in Figure 1. The magnitudes quoted in the SDSS archives are asinh magnitudes (Lupton et al. 1999).

3.1. SEGUE Data at Low Galactic Latitudes

The SEGUE imaging survey is designed to explore the structure of the Milky Way at both high and low Galactic latitudes and, thus, extends to lower latitudes than did the Legacy survey. This extension gives us better leverage on the spatial distribution of stars in the disk components of the Milky Way and on the three-dimensional shape of the stellar halo. Of the 162 SEGUE plates, 86 were targeted off SEGUE imaging, while the remainder were targeted off Legacy imaging. The SEGUE imaging scans are
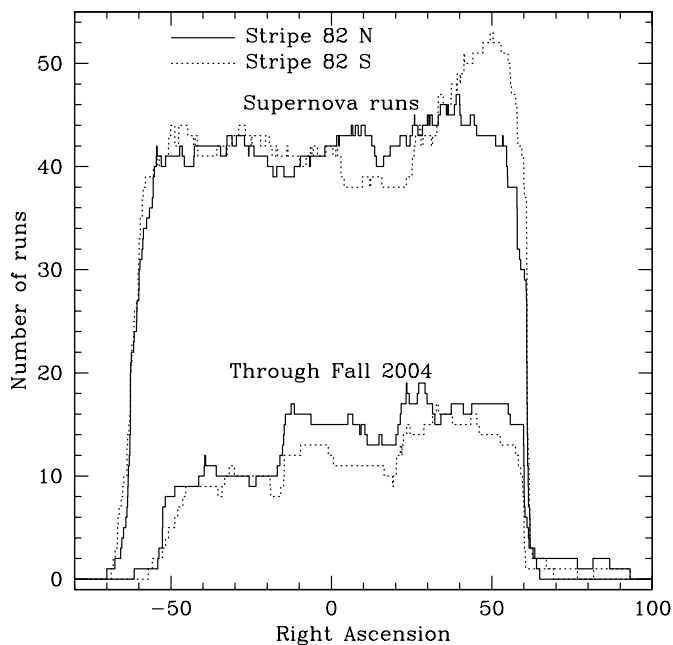
Fig. 2.—Stripe 82, the equatorial stripe in the south Galactic cap, has been imaged multiple times. The bottom pair of curves show the number of scans covering a given right ascension in the north and south strip through the fall of 2004 (these data were also included in DR5); these data are available through the DAS. Since that time, stripe 82 has been covered many more times as part of a comprehensive survey for $0.05 < z < 0.35$ supernovae, although often in conditions of poor seeing, bright moon, and/or clouds; the numbers of additional scans at each right ascension in the north and south strip are indicated in the upper pair of curves. These latter data have not been flux-calibrated. [*See the electronic edition of the Supplement for a color version of this figure.*]

made available in a separate database, termed "SEGUEDR6," within the CAS.

The SEGUE imaging data close to the Galactic plane have regions of higher dust extinction and object density than does the high-latitude SDSS. The SDSS imaging reduction pipelines used to reduce the data for DR6 were not designed for optimal performance in crowded fields and are known to fail for some of these data. In particular

1. When the images are sufficiently crowded, the code has trouble finding suitable isolated stars from which to measure the point-spread function (PSF). Without a suitable determination of the PSF, the brightness measurements by the pipeline (Stoughton et al. 2002) are inaccurate.

2. The pipeline attempts to deblend objects with overlapping images, but the deblend algorithm fails when the number of overlapping objects gets too large, such as happens in sufficiently crowded fields. In such fields, the number of detected objects reported by the pipeline can be a dramatic underestimate.

3. At low latitudes, the dust causing Galactic extinction (as measured by Schlegel et al. 1998, hereafter SFD98) cannot be assumed to lie completely in front of the stars in the sample. This has an effect on the interpretation of quality-assurance tools based on the position of the stellar locus, as we describe below.

Therefore, it is necessary to check that the quality of the reductions in any area of the sky of interest is adequate to address a particular science application of the data.

As Ivezić et al. (2004) and the DR3 paper explain, we use a series of automated quality checks on the imaging data to determine whether the data meet our science requirements; the results of these tests are made available in the CAS. These checks are available for the SEGUE imaging as well. The best indicator of

bad PSF photometry is the difference between PSF and large-aperture magnitudes for stars brighter than 19th magnitude. If the median difference between the two is greater than 0.03 mag, the PSF photometry will not meet the survey requirement of 2% calibration error in g, r, or i. About 2.3% of the fields of the SEGUE imaging data loaded into the CAS in DR6 fail this criterion.[87] For comparison, about 1.6% of all fields in the SDSS Legacy footprint in DR6 fail this criterion.

The automated overall measurement of the quality in a given field also takes into account the location of the stellar locus in the ugr and gri color-color diagrams, and how it differs in each field from the average value over the entire survey (see the discussion in Ivezić et al. 2004). These color-color diagrams are made with SFD98 extinction-corrected magnitudes, so even for very good photometry they may vary from the survey average if that extinction correction is not valid for any reason. The user should apply appropriate caution in interpretation of the stellar locus location diagnostics in the quality assurance for these data.

Finally, the photometric pipeline performs poorly for a stellar density greater than ∼5000 objects brighter than the detection limit per $10' \times 13'$ field, or about 140,000 objects deg^{-2}, a density roughly 10 times the density at high latitudes. The outputs of the photometric pipeline are quite incomplete (and indeed, confusingly, can fall well below 5000 objects per field) and can be unreliable for more crowded fields. Almost all the SEGUE data affected by this problem are in the DAS only; the SEGUE imaging in the CAS (which is the subset used for SEGUE target selection; see below) largely avoids these crowded areas of the sky.

3.2. *SEGUE Target Selection*

SEGUE has as one of its goals a kinematic and stellar population study of the high-latitude thick disk and halo of the Milky Way. The halo is sampled sparsely with a series of tiles each of $7 \ deg^2$ in both the SEGUE imaging stripes and the main Legacy survey area, with centers separated by roughly 10 deg. Each such tile is sampled with two pointings: one plate for stars brighter than $r = 17.8$ (approximately the median target magnitude), and one plate, which typically gets double the standard exposure time, for fainter stars. The target selection categories and criteria are summarized in Table 2 (listed roughly in order from bluest to reddest targets); see the DR4 paper for a description of an earlier version of SEGUE targeting. Most of the target selection categories are sparsely sampled, with a sampling rate that depends on magnitude; see the online documentation for more details. The target selection bits in the primTarget flag are indicated in the table. Spectra with target-selection bits set by the SEGUE target selection algorithm have primTarget bit 0x80000000 and secTarget bit 0x40000000 set.

Half of the science targets on each line of sight are selected using color-color and color-magnitude cuts designed to sample at varying densities across the main sequence from $g - r = 0.75$ (K dwarfs at $T_{eff} < 5000$K). To this sample we add metal-poor main-sequence turnoff stars selected by their blue ugr colors, essentially an ultraviolet excess cut that is highly efficient at separating the halo from the thick disk near the turnoff. At the faint end, $r = 19.5$, the average star that makes this selection is at a heliocentric distance of 10 kpc for $[Fe/H] = -1.54$. To reach to greater distances, we use the strength of the Balmer jump to select field blue horizontal branch (BHB) stars in the ugr color-color diagram (Lenz et al. 1998; Sirko et al. 2004; Clewley et al. 2004). The halo BHB sample extends to distances of 40 kpc at

---

[87] Of course, a much larger fraction of the additional SEGUE data available in the DAS also fail this criterion.

TABLE 2
SEGUE Targeting Algorithms

Category	Bit (Hex)	Color Cuts	No. per Tile
White dwarf	0x80080000	$g < 20.3$, $-1 < g - r < -0.2$, $-1 < u - g < 0.7$, $u - g + 2(g - r) < -0.1$	25
A, BHB stars	0x80020000	$g < 20.5$, $0.8 < u - g < 1.5$, $-0.5 < g - r < 0.2$	≤ 155
Metal-poor MS turnoff	0x80100000	$g < 20.3$, $-0.7 < P_1 < -0.25$, $0.4 < u - g < 1.4$, $0.2 < g - r < 3.0$	200
F/G stars	0x80000200	$14.0 < g < 20.2$, $0.2 < g - r < 0.48$	50
G stars	0x80040000	$14.0 < r < 20.2$, $0.48 < g - r < 0.55$	375
Cool white dwarf	0x80020000	$14.5 < r < 20.5$, $-2 < g - i$, $H_g > \max\,[17.5,\ 16.05 + 2.9(g - i)]$, $g - i < \begin{cases} 0.12, & \text{neighbor with } g < 22 \text{ within } 7'' \\ 1.7, & \text{otherwise} \end{cases}$	10
Low metallicity	0x80010000	$r < 19.5$, $-0.5 < g - r < 0.75$, $0.6 < u - g < 3.0$, $l > 0.135$	150
K giant	0x80040000	$r < 20.2$, $0.7 < u - g < 4.0$, $0.5 < g - r < 0.9$, $0.15 < r - i < 0.6$, $l > 0.07$, $\mu < 0.011''\ \mathrm{yr}^{-1}$	95
K dwarf	0x80008000	$14.5 < r < 19.0$, $0.55 < g - r < 0.75$	95
MS/WD pairs	0x80001000	$15 < g < 20$, $u - g < 2.25$, $-0.2 < g - r < 1.2$, $0.5 < r - i < 2.0$, $-19.78(r - i) + 11.13 < g - r < 0.95(r - i) + 0.5$, $i - z > \begin{cases} 0.5, & \text{if } r - i > 1.0 \\ 0.68(r - i) - 0.18, & \text{otherwise} \end{cases}$	5–10
M subdwarf	0x80400000	$14.5 < r < 19.0$, $g - r > 1.6$, $0.95 < r - i < 1.3$	5
High μ M subdwarf	0x80400000	$\mu > 0.04''\ \mathrm{yr}^{-1}$, $r - z > 1.0$, $15 + 3.5(g - i) > H_r > 12 + 3.5(r - z)$	60
Brown dwarf	0x80200000	$z < 19.5$, $u > 21$, $g > 22$, $r > 21$, $i - z > 1.7$	<5
AGB	0x80800000	$14.0 < r < 19.0$, $2.5 < u - g < 3.5$, $0.9 < g - r < 1.3$, $s < -0.06$	10

Notes.—This table describes Version 4_2 of the SEGUE target-selection algorithm. The hex bit in the second column is set in the primTarget flag. All magnitudes above are PSF magnitudes which have been corrected for Galactic extinction following SFD98. The one exception is the MS/WD pair algorithm, which uses PSF magnitudes without extinction correction. The quantity $l \equiv -0.436u + 1.129g - 0.119r - 0.574i + 0.1984$ is a metallicity indicator following Lenz et al. (1998). The quantities $s \equiv -0.249u + 0.794g - 0.555r + 0.234$ and $P_1 \equiv 0.91(u - g) + 0.415(g - r) - 1.280$ are defined by Helmi et al. (2003). The proper motion μ is in units of arcsec yr^{-1}, and the reduced proper motion is defined as $H_g \equiv g + 5 \log \mu + 5$ and in a similar manner for H_r. The fourth column lists the typical number of targets selected in each category per spectroscopic tile.

$g = 19$ (corresponding to the S/N limit we use for detailed spectroscopic classification; see § 4.3). We select all available BHB candidates in our high-latitude fields and all candidates with $g - r < 0$ irrespective of latitude.

We select distant halo red giant candidates by the photometric offset in the ugr color-color diagram, as quantified by the l color (Lenz et al. 1998; see also Table 2 notes). This offset is caused by their ultraviolet excess and weak Mg ib and MgH at 5175 Å relative to foreground disk dwarfs (Morrison et al. 2001; Helmi et al. 2003). This is augmented by a $3\,\sigma$ proper motion cut using a recalibrated version of the USNO-B catalog (Munn et al. 2004). Spectroscopic identification of true giants using the methodology in Morrison et al. (2003) has shown that the giant selection is roughly 50% efficient at $g < 17$, the current limit to which we can reliably distinguish giants from dwarfs in the spectra. The halo giant sample identified in this way reaches distances of 40 kpc from the Sun. We select candidate low-metallicity stars using a more extreme l-color cut and without any proper motion cut.

The spectroscopic selection also includes smaller categories of rare but interesting objects. These include cool white dwarfs selected with the recalibrated USNO-B reduced proper motion diagram, which can be used to date the age of the Galactic disk (Gates et al. 2004; Harris et al. 2006), high proper motion targets from the SUPERBLINK catalog (Lépine & Shara 2005), which have uncovered some of the most extreme M subdwarfs known (Lépine et al. 2007) and have aided in the calibration of their metallicity scale using common proper motion pairs, and white dwarf/main-sequence binaries containing cool white dwarfs, which are predicted to be the dominant population among this type of binaries (Schreiber & Gänsicke 2003). These rare object categories also include color-only selections for cool subdwarfs, brown dwarfs (using cuts similar to those employed by Chiu et al. 2006), and the SEGUE "AGB" (asymptotic giant branch) category that selects metal-rich, cool giants that separate readily from the ugr stellar locus.

Table 2 describes Version 4_2 of the SEGUE target-selection algorithms. The algorithms have evolved throughout the survey, and users wishing to understand the detailed selection associated with each target category should examine the SEGUE documentation off the DR6 survey page. The user should also know that SEGUE target selection has been run only on those chunks used to design SEGUE plates and has not yet been run on the bulk of the Legacy survey imaging.

3.3. A Caveat on High Proper Motion Stars

As described in the DR2 paper, the proper motions of stars in the SDSS are taken from the measurements of the USNO-B1.0 (Monet et al. 2003), based primarily on the POSS-I and POSS-II. However, this catalog is incomplete at the highest proper motions, greater than 100 milliarcseconds yr^{-1}. Confusingly, objects with no proper motion measurement in the USNO-B1.0 catalog have their proper motion listed as 0.0 in the CAS ProperMotions table, meaning that a query for *low* proper motion stars will be contaminated by a small number of the highest proper motion stars. The best available catalog of high proper motion stars can be found in the SUPERBLINK catalog of Lépine & Shara (2005) and references therein; we hope to incorporate this catalog into the proper motion data in the SDSS in future data releases.

3.4. Low Galactic Latitude SDSS Commissioning Data

During commissioning and subsequent tests of the SDSS observing system, additional data were obtained outside of the nominal survey region. These data consist of 28 runs (see Table 1 of Finkbeiner et al. 2004) at low Galactic latitude, mostly in the star-forming regions of Orion, Cygnus, and Taurus. There are 832 deg^2 of data, 470 deg^2 of which have been previously released[88] as flat files. There are three types of files: calibrated

[88] Available online at http://photo.astro.princeton.edu.

images (one calibImage per field), calibrated object files (one calibObj per field), and condensed "sweep" files (one star or galaxy file per run/camcol).

The remaining 362 deg² are hereby released in the same format, but they are not available in the DAS or CAS. These data have been photometrically calibrated using the übercalibration algorithm (§ 3.5).[89] Übercalibration takes advantage of the Apache Wheel calibration scans (not shown in Fig. 1) to tie the photometry of disjoint regions of the sky together; nevertheless, because the overlap with other runs is less than in the main survey area, their calibration may not be quite as good.

3.5. *Improved Photometric Calibration*

Photometric calibration in SDSS has been carried out in two parallel approaches. The first uses an auxiliary 20″ photometric telescope (PT) at the site, which continuously surveys a series of US Naval Observatory standard stars which are used to define the SDSS $u'g'r'i'z'$ photometric system (Smith et al. 2002). Transformations between the $u'g'r'i'z'$ and native SDSS 2.5 m $ugriz$ photometric systems and zero points for stars in patches surveyed by the 2.5 m telescope are determined with these data (Tucker et al. 2006; Davenport et al. 2007). These secondary patches are spaced roughly every 15° along the imaging stripes. This approach has allowed the SDSS photometry to reach its goals of calibration errors with an rms of 2% in g, r, and i, and 3% in u and z (Ivezić et al. 2004), as measured from repeat scans (see the discussion in Ivezić et al. 2007). This is the calibration process that has been used in all data releases to date. However, it is not ideal for several reasons.

1. The $u'g'r'i'z'$ filter system of the PT camera is subtly different from the $ugriz$ system on the 2.5 m.
2. There are persistent problems with the flat fielding of both the PT and 2.5 m cameras, especially in u'.
3. No use is made of overlap data in the 2.5 m scans to tie the zero points together.

A second approach, termed "übercalibration" (Padmanabhan et al. 2007) does not use information from the PT to calibrate individual runs, but rather uses the overlaps between the 2.5 m imaging runs to tie the photometric zero points of individual runs together and measure the 2.5 m flat fields and to determine the extinction coefficients on each night. Unlike the standard PT calibrations, übercalibration explicitly assumes that the photometric calibration parameters (a zero point for each CCD and atmospheric extinction linear with air mass) are constant through a photometric night. This assumption appears justified, as the resulting calibration has errors of ~1% in g, r, i, and z, and 2% in u, roughly a factor of 2 below those of the standard processing, as determined from the overlaps themselves and from the measurement of the "principal colors" of the stellar locus (see the discussion in Ivezić et al. [2004] and the DR3 paper). This scatter is dominated by unmodeled variations in the atmospheric conditions in the site, including changes in the atmospheric extinction through a night.

The relative calibration of the photometric scans via overlaps does not determine the photometric zero points in the five filters. The zero points are constrained in practice by forcing the übercalibrated photometry of bright stars to agree in the mean with that calibrated in the standard way (Tucker et al. 2006). Thus,

this work does not represent an improvement in the calibration of the SDSS photometry to a true AB system (in which magnitudes can be translated directly into physical flux units); see the discussion in the DR2 paper, Eisenstein et al. (2006), and Holberg & Bergeron (2006). Moreover, there are subtle differences between the response of the six filters in each row of the SDSS camera, especially in z (see the discussion in Ivezić et al. 2007); these differences have not been corrected.

Both versions of SDSS photometry are now made available through the CAS in DR6. The PT-calibrated photometry for each detected object is stored in the database in the same tables and columns as in DR5, and both the offset between PT and übercalibration, as well as the übercalibrated magnitudes, are stored in the UberCal table of the CAS. Database functions are available to apply these offsets and output übercalibrated photometry. The distribution of these offsets is shown in Figures 15 and 16 of Padmanabhan et al. (2007); the improvements are subtle, changing magnitudes of most individual objects by 0.02 mag or less.

3.6. *The Photometry of Bright Galaxies*

Because of scattered light (see the EDR paper), the background sky in the SDSS images is nonuniform on arcminute scales. The photometric pipeline determines the median sky value within each 101.4″ (256 pixel) square on a grid with 50.7″ spacing, and bilinearly interpolates this sky value to each pixel. This procedure overestimates the sky near large extended galaxies and bright stars, causing a systematic decrease in the number density of faint objects near bright galaxies (see the discussion in the DR4 paper and Mandelbaum et al. 2005). In addition, it also strongly affects the photometry of bright galaxies themselves, as has been reported by Lauer et al. (2007), Bernardi et al. (2007), and Lisker et al. (2007). We have quantified this effect by adding simulated galaxies with exponential and de Vaucouleurs (1948) profiles to SDSS images, following Blanton et al. (2005a). The simulated galaxies ranged from apparent magnitude $m_r = 12$–19 in half-magnitude steps, with a one-to-one mapping from m_r to Sérsic half-light radius determined using the mean observed relation between these quantities for MAIN sample galaxies (Strauss et al. 2002) with exponential and de Vaucouleurs profiles. Axis ratios of 0.5 and 1 were used, with random position angles for the noncircular simulated galaxies. The results in the r band are shown in Figure 3, plotting the difference between the input magnitude and the model magnitude returned by the SDSS photometric pipeline as a function of magnitude. Also shown is the fractional error in the scale size r_e. The biases are significant to $r = 16$ for late-type galaxies and to $r = 17.5$ for early-type galaxies. J. B. Hyde & M. Bernardi (2007, unpublished) fit de Vaucouleurs models to SDSS images of extended elliptical galaxies, using their own sky-subtraction algorithm, which is less likely to overestimate the sky level near extended sources. Their results, also shown in the figure, are quite consistent with the simulations.

The scatter in the offset from one realization to another is large enough that we cannot recommend a deterministic correction for this problem. This scatter depends in part on the position of the simulated galaxy relative to the grid on which the sky interpolation occurs. We are working on an improved algorithm which will fit the extended profiles of galaxies explicitly as part of the sky determination, and hope to include the results in a future data release.

4. SPECTROSCOPY

The Sixth Data Release contains a number of improvements and additions to the SDSS spectroscopy. These include an improved

---

[89] The current übercalibration has yielded calibrations typically 0.02 mag different from those previously released, but some runs/camera columns show differences as large as 0.05 mag. The variance within each field is also somewhat reduced by correcting flat-field errors at the 0.01 or 0.02 mag level.
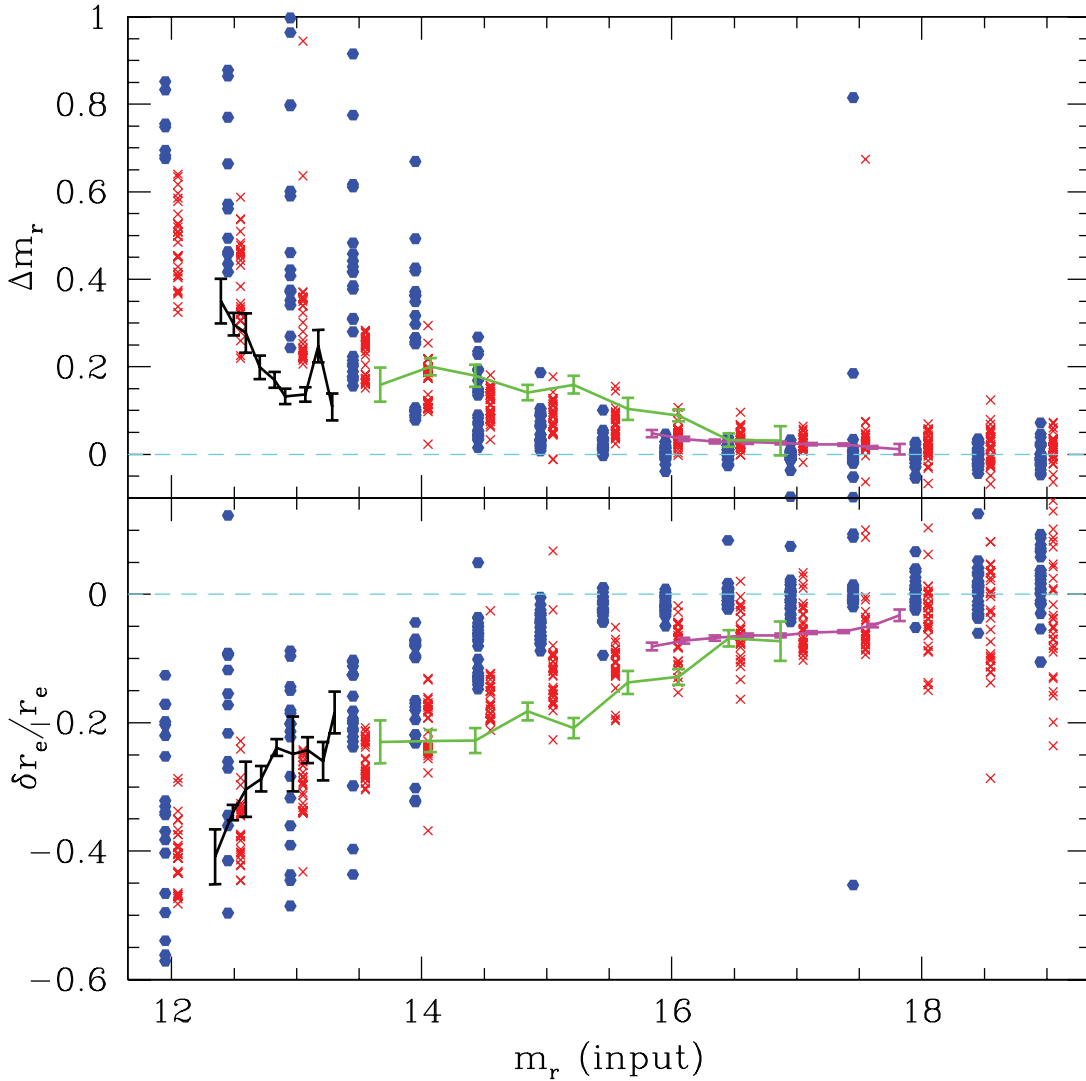
Fig. 3.— Effects of sky subtraction errors on the photometry of bright galaxies. *Top*: Error in the *r*-band model magnitude of simulated galaxies with an $n = 1$ (exponential) profile (*blue hexagons*) and an $n = 4$ (de Vaucouleurs) profile (*red crosses*) as determined by the photometric pipeline, as a function of magnitude. There are 15 galaxies simulated at each magnitude for each profile. Also shown are the analogous results from J. B. Hyde & M. Bernardi (2007, unpublished) for three early-type galaxy samples: 54 nearby ($z < 0.03$) early-type galaxies from the ENEAR catalog (da Costa et al. 2000) in black; 280 brightest cluster galaxies from the C4 catalog (Miller et al. 2005) in green; and 9000 early-type galaxies from the Bernardi et al. (2003a) analysis in magenta. *Bottom*: Fractional error in the scale size r_e as a function of magnitude from the simulations and the J. B. Hyde & M. Bernardi analysis.

pipeline to extract and calibrate the one-dimensional spectra (§ 4.1), the results of an independent pipeline to classify objects and measure redshifts (§ 4.2), the results of a pipeline to determine the effective temperatures, gravities and metallicities of stars (§ 4.3), and improvements to the existing code to measure velocity dispersions (§ 4.4).

4.1. *The Extraction and Calibration of One-dimensional Spectra*

The pipeline that extracts, combines, and calibrates the SDSS spectra of individual objects from the two-dimensional spectrograms (`idlspec2d`) was originally designed to obtain meaningful redshifts for galaxies and quasars. However, there were several ways in which the code was inadequate, especially in light of the stellar focus of the SEGUE project, and the recognition of the rich stellar data available among the spectra of the main SDSS survey. The spectrophotometry was tied to the fiber magnitudes of stars, whose relation to the true, PSF magnitudes of stars is seeing dependent. In addition, the SEGUE spectros-

copy includes "bright plates" which contain substantial numbers of stars as bright as $i_{\rm fiber} = 14.2$, and scattered light from these stars caused systematic errors in the sky subtraction on these plates. Finally, there were errors in the wavelength calibration as large as $15 \ {\rm km \ s^{-1}}$ on some plates, acceptable for most extragalactic science, but a real limitation for SEGUE's science goals. These concerns and others have caused us to substantially revise and improve the `idlspec2d` pipeline; the results of this improvement are included in DR6.

4.1.1. *Spectrophotometry: Flux Scale*

The new code has a different spectrophotometric calibration flux scale. The fiber magnitude reported by the photometric pipeline is the brightness of each object, as measured through a $3''$ diameter aperture corrected to $2''$ seeing to match the entrance aperture of the fibers (see the discussion in the EDR paper). However, the relationship between the fiber magnitudes of stars and the PSF magnitudes (which, for unresolved objects, is our best determination of a true, total magnitude) is dependent on seeing;
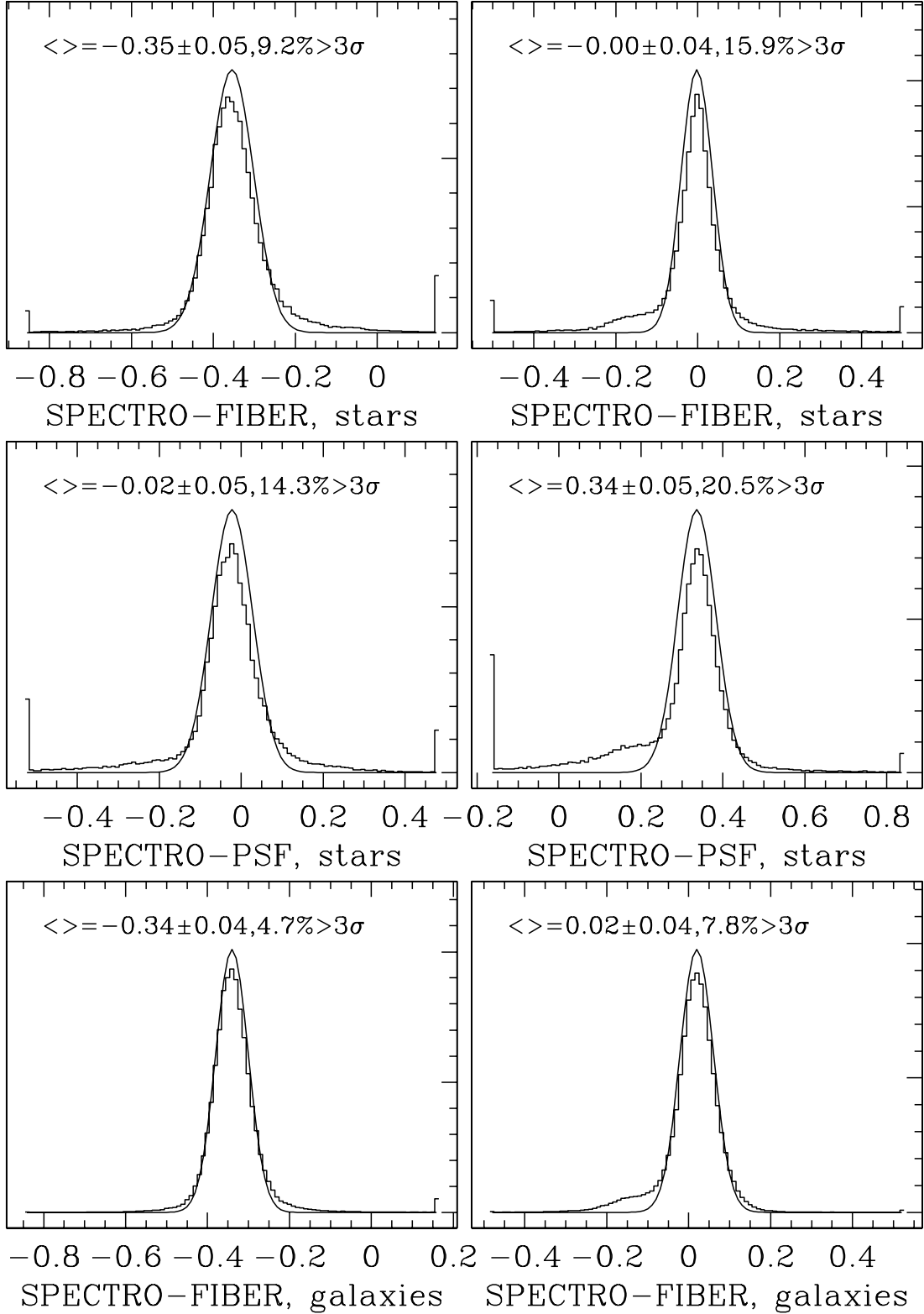
FIG. 4.—Distribution of differences between *r*-band photometry synthesized from SDSS spectra (labeled SPECTRO), and PSF and fiber magnitudes, for stars and galaxies; results are shown for DR6 (*left*) and the previous version of the calibration available in DR5 (*right*). Only objects with PSF magnitude brighter than 19 are shown. The most important difference is the offset of 0.35 mag between the two, due to the change in calibration from fiber to PSF photometry. Each panel includes the mean and standard deviation of the best-fit Gaussian, as well as the number of objects lying beyond 3 σ (as a measure of the non-Gaussianity of the tails). Results are shown for *r* band, but *g*- and *i*-band results are very similar.

Plate	MJD	Plate	MJD	Plate	MJD	Plate	MJD
269............................	51910	345............................	51690	460............................	51924	683............................	52524
270............................	51909	349............................	51699	492............................	51955	730............................	52466
277............................	51908	353............................	51703	543............................	52017	830............................	52293
284............................	51943	367............................	51997	554............................	52000	872............................	52339
309............................	51666	394............................	51913	556............................	51991	1394..........................	53108
324............................	51666	403............................	51871	616............................	52374	1414..........................	53135
336............................	51999	446............................	51899	616............................	52442	1453..........................	53084

NOTE.—The second column lists the Modified Julian Date (MJD) on which each plate was observed.

this is made worse because the *colors* of stars measured via fiber magnitudes will be sensitive to the different seeing in the different filters (although cases in which the seeing is dramatically different in the different bands are fairly rare). With this in mind, the pipeline used in DR6 determines the spectrophotometric calibration on each plate such that the flux of the spectrum of standard stars integrated over the filter curve matches the PSF magnitude of the stars as measured from their imaging. This calibration is determined for each of the four cameras (two in each spectrograph) from observations of standard stars. Additional corrections to handle large-scale astrometric and chromatic terms are measured from isolated stars and galaxies of high S/N and are then applied to all the objects on the plate.

The results of this calibration may be seen in Figure 4, which compares synthesized magnitudes from the SDSS spectra with the PSF and fiber magnitudes in the imaging data, showing results from both the old ("DR5") and new ("DR6") codes. We emphasize that the calibration is *not* tied to the PSF photometry of each object individually (otherwise the comparison in Fig. 4 would be a tautology); there is a single calibration determined for each camera in a given plate. This means, for example, that it is meaningful to compare photometry and spectrophotometry of individual objects to look for variability (e.g., Vanden Berk et al. 2004).

The PSF includes light that extends beyond the $3''$ diameter of the filters, and thus, the PSF-calibrated spectrophotometry is systematically *brighter* than the old fiber-calibrated photometry by the difference between PSF and fiber magnitudes, which is roughly 0.35 mag (albeit dependent on seeing). Again, because the PSF photometry represents an accurate measure of the brightness of stars, this calibration means that the spectrophotometry matches the PSF photometry for stars to an rms of 4%. This distribution does show an extended tail presumably caused by blended and variable objects,[90] but the distribution is substantially more symmetric than for the previous version of the pipeline. Interestingly, for galaxies, the rms difference between spectroscopic photometry and the fiber magnitudes is also 4%. The previous code shows a similarly narrow distribution, albeit with larger tails. The distribution of the difference of the $g - r$ and $r - i$ colors between PSF photometry and as synthesized from the spectrophotometry again shows a narrow core in both DR5 and DR6, but with less extensive non-Gaussian outliers with the new code.

Because of errors in the processing step, there are 28 plates, listed in Table 3, that were calibrated using fiber magnitudes rather than PSF magnitudes. Therefore, objects on these plates have a spectroscopic flux scale systematically lower by 0.35 mag

[90] Indeed, the fiber magnitudes include light from overlapping blended objects, thus the tails are less extensive in the fiber magnitude comparison.

than the rest of the survey. These will be processed correctly in a subsequent data release.

4.1.2. *Spectrophotometry: Wavelength Dependence*

As discussed in the DR2 paper, each plate includes observations of a number of spectrophotometric standards, typically F subdwarfs. Their observed spectra are fit to and calibrated against the models of Gray & Corbally (1994), as updated by Gray et al. (2001). We can compare the spectrophotometric calibration between DR5 and DR6 by plotting the ratio of the summed spectra of these standard stars on each plate as determined by the two versions of the pipeline. The 0.35 mag overall flux scale between the two calibrations has been taken out by forcing all the curves through unity at 6200 Å. The median ratio (as determined from 1278 plates) and the 68.3% and 95.4% outliers are shown in Figure 5. The median ratio differs from unity by less than 5% at all wavelengths, but a small fraction of the plates have differences as large as 30% at the far blue end.

Do these changes represent an improvement scientifically? Figure 4 of the DR2 paper quantified the uncertainties in the spectrophotometric calibration used at that time by looking at the
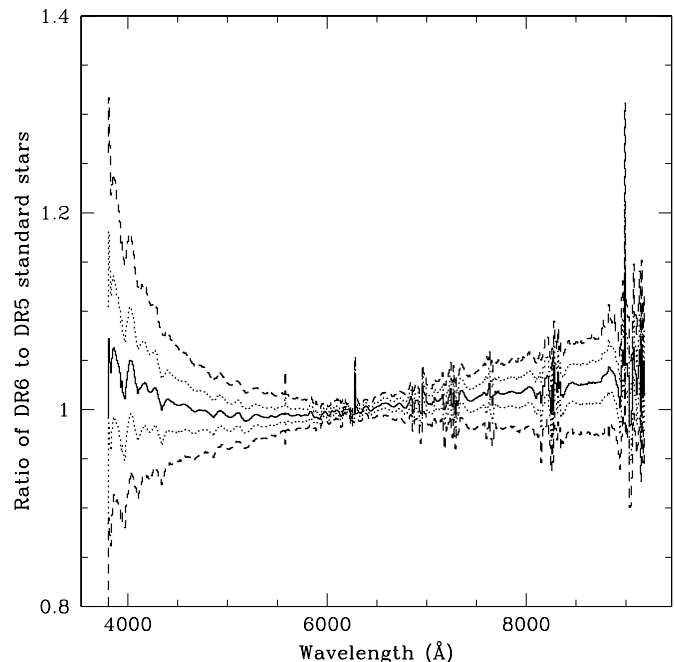

FIG. 5.—Ratio of the summed spectra of standard stars on each plate as determined by the DR6 and DR5 versions of spectrophotometry, rescaled to unity at 6200 Å. The solid line is the median ratio spectrum over 1278 plates, the dotted lines enclose 68.3% of the plates (corresponding to 1 σ for a Gaussian distribution), and the dashed lines enclose 95.4% of the plates (corresponding to 2 σ). The distribution at each wavelength is in fact close to Gaussian.
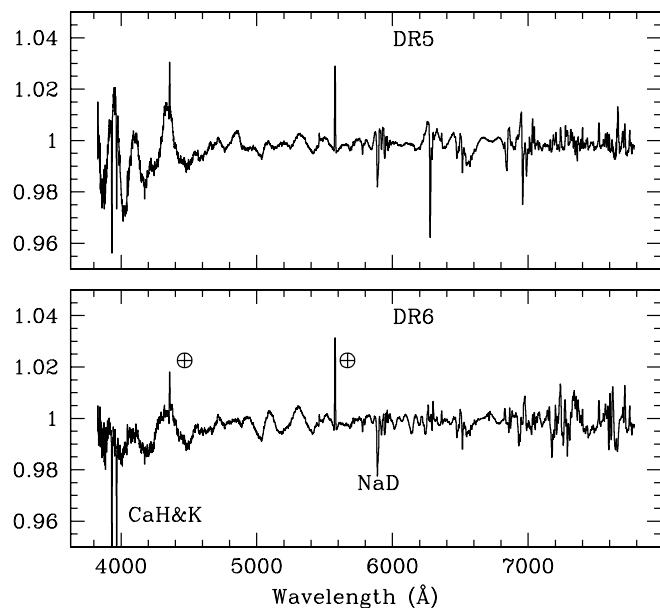
Fig. 6.—Median ratio of observed flux-calibrated spectra of luminous red elliptical galaxies to their averaged spectra (after taking evolution into account), for the previous (DR5) and current (DR6) spectroscopic reductions. This quantifies the wavelength dependence of systematic errors in the spectrophotometric calibration; the amplitude of these features, already small in the previous reductions, have been reduced further in DR6, especially in the blue. The features at Ca H and K and at Na D are probably due to absorption from the interstellar medium. The strong features at the sky lines at 5577 and 4358 Å marked with a circled plus sign are related to the S/N of the spectra; a similar analysis with quasar spectra shows these features to have substantially lower amplitude.

Fig. 7.—Blue part of the spectrum of an A0 BHB star, SDSS J004037.41+ 240906.5, as given by the old (*dotted curve*) and new (*solid curve*) versions of `idlspec2d`. The old curve has been scaled up to reflect the difference in the calibration of the two reductions. The synthetic spectrum, shown as a dashed curve, is generated from a model with parameters matching those derived from the SSPP ($T_{eff} = 8500$ K, $\log g = 3.25$, [Fe/H] $= -2.00$). The continuum between the absorption lines is much smoother and matches the synthetic spectrum much better for the new reductions than for the old. The synthetic spectrum has been normalized to match the observed spectrum at 4500 Å. Neither the model nor the spectra have been corrected for Galactic reddening [which is $E(B - V) = 0.036$ in this line of sight]. [*See the electronic edition of the Supplement for a color version of this figure.*]

mean fractional offset between observed spectra of white dwarfs and best-fit models for them. Figure 6 shows a similar analysis with the old and new reductions. The curves show the median fractional difference between a sample of 128,000 calibrated luminous red galaxy (LRG; Eisenstein et al. 2001) spectra and a model based on averaged observed LRG spectra that is allowed to evolve smoothly with redshift (see the discussion in § 3 of the DR5 paper). Because the LRGs have a broad range of redshifts, one expects no feature specific to the LRGs to appear in this plot as a function of observed wavelength, and deviations from unity are a measure of the small-scale errors in the spectrophotometry. There are systematic oscillations at the 2% level in the DR5 reductions. These wiggles correspond to positions of strong absorption lines in the standard stars, especially in the vicinity of the 4000 Å break in the blue. This is now handled by not fitting the instrumental response to any residual nontelluric features finer than 25–50 Å, as the response is not expected to vary on those scales. This reduces the amplitude of the wiggles by a factor of 2 in the DR6 reductions, especially at the blue end. Redward of 4500 Å, 50% of the spectra fall within 3% of the median value; this increases to 7% at 3800 Å. The features at Ca K and H (3534 and 3560 Å) and Na D (5890 and 5896 Å) are probably due to absorption from the interstellar medium (although the latter probably has a contribution from sky line residuals). The sky line residuals (marked with a circled plus sign) are a function of S/N; a similar analysis with higher S/N quasars shows substantially smaller residuals at the strong sky lines.

The effect of this improvement in the spectrophotometric calibration becomes clear if we examine the spectra of individual stars. Figure 7 shows the blue part of the spectrum of an A0 BHB star as calibrated with the old code (*dotted line*) and the new (*solid line*), together with a synthetic spectrum based on the atmospheric parameters estimated by the SEGUE Stellar Pa-
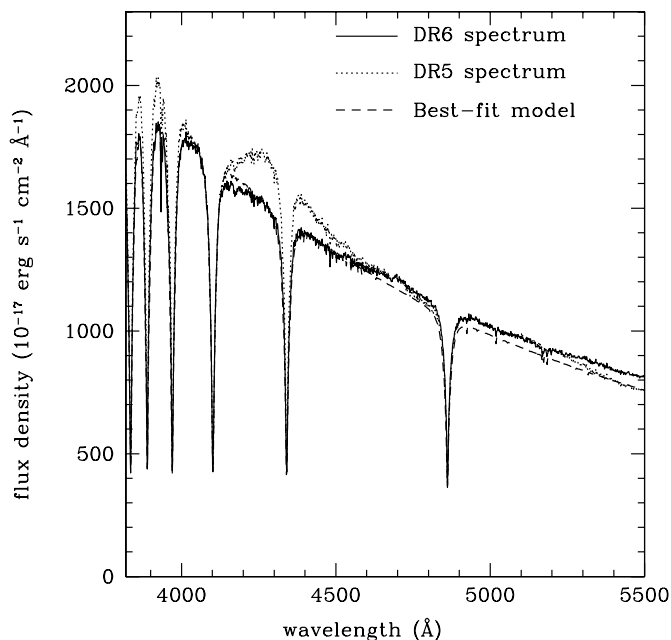
rameter Pipeline (§ 4.3; $T_{eff} = 8446$ K, $\log g = 3.15$, [Fe/H] $= -1.96$). The new reductions are clearly smoother between the absorption lines; the match between the DR6 calibrated spectrum and the synthetic spectrum is also superior.

4.1.3. *Radial Velocities*

In order to measure the dynamics of the halo of the Milky Way, SEGUE requires stellar radial velocities accurate to 10 km s^{-1}, significantly more demanding than the original SDSS requirements of 30 km s^{-1}. The previous version of `idlspec2d` had systematic errors of 10–15 km s^{-1} in the wavelength calibration because of a dearth of strong lines at the blue end of the spectrum in the calibration lamps and in the nighttime sky. The skyline fits for the blue-side wavelength corrections now use a more robust algorithm allowing less freedom in the fits, and these problems are largely under control.

We monitor the systematic and random errors in the radial velocities in the SEGUE data by comparing repeat observations on the bright and faint plates of each SEGUE pointing. The duplicate observations consist of roughly 20 "quality-assurance" objects selected at the median magnitude of the SEGUE data, as well as a similar number of spectroscopic calibration objects that are observed on both plates. The mean difference in the measured radial velocities between the two observations of the quality assurance objects depends on stellar type, with a standard deviation of 9 km s^{-1} for A and F stars and 5 km s^{-1} for K stars.[91] The mean radial velocity offset between the two plates in each pointing, as measured using all the duplicate observations,

---

[91] Thus, the error on a single star is $\sqrt{2}$ less than these values.

TABLE 4
REDSHIFT WARNING FLAGS FROM specBS

Bit	Name	Comments
0..............................	SKY_FIBER	Fiber is used to determine sky; there should be no object here.
1..............................	SMALL_LAMBDA_COVERAGE	Because of masked pixels, less than half of the full wavelength range is reliable in this spectrum.
2..............................	CHI2_CLOSE	The second best-fitting template had a reduced χ^2 within 0.01 of the best fit (common in low S/N spectra).
3..............................	NEGATIVE_TEMPLATE	Synthetic spectrum is negative (only set for stars and QSOs).
4..............................	MANY_5SIGMA	More than 5% of pixels lie more than 5 σ from the best-fit template.
5..............................	CHI2_AT_EDGE	χ^2 is minimized at the edge of the redshift-fitting region (in this circumstance, Z_ERR is set to -1).
6..............................	NEGATIVE_EMLINE	A quasar emission line (C IV, C III], Mg II, Hβ, or Hα) appears in absorption with more than 3 σ significance due to negative eigenspectra.

suggests systematic velocity errors from plate to plate of only 2 km s^{-1} rms.

We have checked the zero point of the overall radial velocity scale (as measured using the ELODIE templates in the specBS code; see the discussion in § 4.2) by carrying out high-resolution observations of 150 SEGUE stars. This has revealed a systematic error of 7.3 km s^{-1} (in the sense that the specBS velocities are too low) due to subtly different algorithms in the line fits to arc and sky lines. This has been fixed in the output files of the SEGUE Stellar Parameter Pipeline (§ 4.3), but has *not* yet been fixed elsewhere in the CAS. The improved wavelength calibration leads to smaller sky subtraction residuals for many objects, especially noticeable in the far red of the spectrum.

4.1.4. *Additional Outputs*

Under good conditions, a typical spectroscopic plate is observed three times in exposures of 15 minutes each; more exposures are added in poor conditions to reach a target S/N in the spectra. The idlspec2d pipeline stitches together the resulting individual spectra to determine the final spectrum of a given object. However, for the most accurate determination of the noise characteristics of the spectra (for example, in detailed analyses of the Lyα forest of quasars; see the discussion in McDonald et al. 2006) or to determine whether a specific unusual feature in a spectrum is real, it is desirable to go back to the uncombined spectra. These uncombined spectra are now made available for every plate in the so-called spPlate files through the DAS.

The published spectra have had a determination of the spectrum of the foreground sky subtracted from them. The sky is measured in 32 fibers (64 fibers for the faint SEGUE plates) placed in regions where no object has been detected to 5 σ in the imaging data, interpolated (both in amplitude and in wavelength, allowing for some undersampling) to each object exposure, and subtracted. However, it is often useful to see the sky spectrum that has been subtracted from each object, for example, to study the nature of extended foreground emission-line objects in the data (e.g., see Hewett et al. [2003] for the discovery of a 2° diameter planetary nebula in the SDSS data). The sky spectrum subtracted from each object spectrum is now available through both the DAS and the CAS.

4.1.5. *The Treatment of Objects with Very Strong Emission Lines*

There is a known problem, which is not fixed with the current version of idlspec2d, whereby the code that combines the individual 15 minute exposures will occasionally misinterpret the peaks of particularly strong and narrow emission lines as cosmic rays and remove them. All pixels affected by this have the inverse variance (i.e., the inverse square of the estimated error at this pixel) set to zero, indicating that the code recognizes that the pixel in question is not valid. A diagnostic of this problem is unphysical line ratios in the spectra of dwarf starburst galaxies, as the tops of the strongest lines are artificially clipped. This is a rare problem, affecting less than 1% of galaxies with rest equivalent width in the Hβ line greater than 25 Å, but users investigating the properties of galaxies with strong emission lines should be aware of it. We hope to fix this problem in the next data release.

4.2. *An Independent Determination of Spectral Classifications and Redshifts*

As described in the EDR paper and Subbarao et al. (2002), the spectral classifications and radial velocities available in the data releases have been based on a code (spectro1d) that cross-correlates the observed spectra with a variety of templates in Fourier space to determine absorption-line redshifts and fits Gaussians to emission lines to determine emission-line redshifts. A completely separate code, termed specBS and written by D. Schlegel (in preparation), instead carries out χ^2 fits of the spectra to templates in wavelength space (in the spirit of Glazebrook et al. 1998), allowing galaxy and quasar spectra to be fit with linear combinations of eigenspectra and low-order polynomials. Stellar radial velocities are fit both to SDSS-derived stellar templates and to templates drawn from the high-resolution ELODIE (Prugniel & Soubiran 2001) library. The spectro1d outputs give the default spectroscopic information available through the CAS, but the specBS outputs are made available through the CAS for the first time with DR6.[92] While spectro1d uses manual inspection to correct the redshifts and classifications of a small fraction of its redshifts, specBS is completely automated.

Tests show that the two pipelines give impressively consistent results. At high S/N, the rms difference between the redshifts of the two pipelines is of order 7 km s^{-1} for stars and galaxies, although the spectro1d redshifts are systematically higher by 12 km s^{-1} due to differences in the templates. The difference distribution has non-Gaussian tails, but as a test of catastrophic errors, we find that 98% of *all* objects with spectra (after excluding the blank sky fibers) have consistent classification (star, quasar, galaxy) and redshifts agreeing within 300 km s^{-1} for galaxies and stars and 3000 km s^{-1} for quasars.

Half of the remaining 2% are objects of very low S/N, and the other half are a mixture of a variety of unusual objects, including BL Lacertae objects (Collinge et al. 2005; their lack of spectral features makes it unsurprising that the two pipelines come to different conclusions), unusual white dwarfs, including strong magnetic objects and metal-rich systems (Schmidt et al. 2003; Eisenstein et al. 2006; Dufour et al. 2007), unusual broad absorption line quasars (Hall et al. 2002), superposed objects,

---

[92] The outputs of specBS have also been made publically available through the NYU Value-Added Galaxy Catalogue; see Blanton et al. (2005b).

TABLE 5
OUTPUTS OF THE specBS PIPELINE MADE AVAILABLE IN THE DR6 CAS

Parameter	Comments
CLASS	STAR, GALAXY, or QSO
SUBCLASS	Stellar subtype, galaxy type (star forming, etc.)
Z	Heliocentric redshift
Z_ERR	Error in redshift
RCHI2	Value of reduced χ^2 for template fit to spectrum
DOF	Degrees of freedom in χ^2 fit
VDISP	Velocity dispersion for galaxies (km s^{-1})
VDISP_ERR	Error in velocity dispersion (km s^{-1})
ZWARNING	Set if the classification or redshift are uncertain; see Table 4
ELODIE_SPTYPE	Spectral type of best-fit ELODIE template
ELODIE_Z	Redshift determined from best-fit ELODIE template
ELODIE_Z_ERR	Error in redshift determined from best-fit ELODIE template

including at least one gravitational lens (Johnston et al. 2003), and so on. Both pipelines set flags when the classifications or redshifts are uncertain (see Table 4); the majority of these discrepant cases are flagged as uncertain by both pipelines.

Table 5 lists the outputs from the specBS pipeline included in the CAS for each object. In addition, the DAS includes the results of the cross-correlation of each of the templates with each spectrum, as well as Gaussian fits to the emission lines. These quantities are included in the SEGUE Stellar Parameter Pipeline table (§ 4.3) in the CAS and as flat files in the DAS.

4.3. The Measurement of Stellar Atmospheric Parameters from the Spectra

The SEGUE science goals require accurate determinations of effective temperature ($T_{\rm eff}$), surface gravity ($\log g$, where g is in cgs units, cm s^{-2}), and metallicity ([Fe/H]), for the stars with spectra (and *ugriz* photometry) obtained by SDSS. We have developed the SEGUE Stellar Parameter Pipeline (SSPP), to determine these quantities and measure 77 atomic and molecular line indices for each object. The code and its performance are described in detail by Lee et al. (2007a). Validation of the sets of parameters based on Galactic open and globular clusters and with high-resolution spectroscopy obtained for over 150 SDSS/SEGUE stars is discussed by Lee et al. (2007b) and Allende Prieto et al. (2007). Because of the wide range of parameter space covered by the stars that are observed, a variety of techniques are used to estimate the atmospheric parameters; a decision tree is implemented to decide which methods or combination of methods provide optimal measures, based on the colors of the stars and S/N of the spectra.

These methods include the following.

1. Fits of the spectra to synthetic photometry and continuum-corrected spectra based on R. L. Kurucz (1993, private communication) model atmospheres (Allende Prieto et al. 2006), or to synthetic spectra computed with the more recent Castelli & Kurucz (2003) models (Lee et al. 2007a).

2. Measurements of the equivalent widths of various metal-sensitive lines, including the Ca II K line (Beers et al. 1999) and the Ca II infrared triplet (Cenarro et al. 2001).

3. Measurements of the equivalent widths of various gravity-sensitive lines such as Ca I $\lambda4227$ Å and the 5175 Å Mg I *b*/MgH complex (e.g., Morrison et al. 2003).

4. Measurements of the autocorrelation function of the spectrum, which is useful for high-metallicity stars (Beers et al. 1999).

5. A neural network technique which takes the observed spectrum as input, trained on previously available parameters from the SSPP (Re Fiorentin et al. 2007).

For stars with temperatures between 4500 and 7500 K and with average S/N per spectral pixel greater than 15, the typical formal errors returned by the code are $\sigma(T_{\rm eff}) = 150$ K, $\sigma(\log g) = 0.25$ dex, and $\sigma([{\rm Fe/H}]) = 0.20$ dex. Comparison with 150 stars with high S/N, high-resolution spectra (and therefore reliable stellar parameters) validates these error estimates, at least for those stars with the highest quality SDSS spectra.

The SSPP assumes solar abundance ratios when quoting metallicities, with the caveat that several of the individual techniques (those that involve the Ca and Mg line strengths) adopt a smoothly increasing [α/Fe] ratio, from 0.0 to +0.4, as inferred metallicity decreases from solar to [Fe/H] = -1.5. Other techniques, which are based on regions of the spectra dominated by lines from unresolved Fe-peak elements, do not assume such relationships.

The S/N limit for acceptable estimated stellar parameters varies with each individual method employed by the SSPP. As a general rule, the SSPP sets a conservative criterion that the average S/N per pixel over the wavelength range 3800–6000 Å must be greater than 15 for stars with $g - r < 0.3$, and greater than 10 for stars with $g - r \geq 0.3$. Stars of low S/N do not have their parameters reported by SSPP. Table 5 of Lee et al. (2007a) describes the valid ranges of effective temperature, $g - r$ color, and S/N for each method used in the SSPP. The SSPP values are combined with the outputs of specBS (§ 4.2) and are loaded as a single table into the CAS, with entries for every object with a spectrum.

For the coolest stars, measuring precise values of $T_{\rm eff}$, $\log g$, and [Fe/H] from spectra dominated by broad molecular features becomes extremely difficult (e.g., Woolf & Wallerstein 2006). As a result, the SEGUE SSPP does not estimate atmospheric parameters for stars with $T_{\rm eff} < 4500$ K, but instead estimates the MK spectral type of each star using the Hammer spectral typing software developed and described by Covey et al. (2007).[93] The Hammer code measures 28 spectral indices, including atomic lines (H, Ca I, Ca II, Na I, Mg I, Fe I, Rb, and Cs) and molecular band heads (G band, CaH, TiO, VO, and CrH) as well as two broadband color ratios. The best-fit spectral type of each target is assigned by comparison to the grid of indices measured from more than 1000 spectral type standards derived from spectral libraries of comparable resolution and coverage (Allen & Strom 1995; Prugniel & Soubiran 2001; Hawley et al. 2002; Bagnulo et al. 2003; Le Borgne et al. 2003; Valdes et al. 2004; Sánchez-Blázquez et al. 2006). These indices and the best-fit type from the

---

[93] The Hammer code has been made available for community use; the IDL code can be downloaded from http://www.cfa.harvard.edu/~kcovey/thehammer.
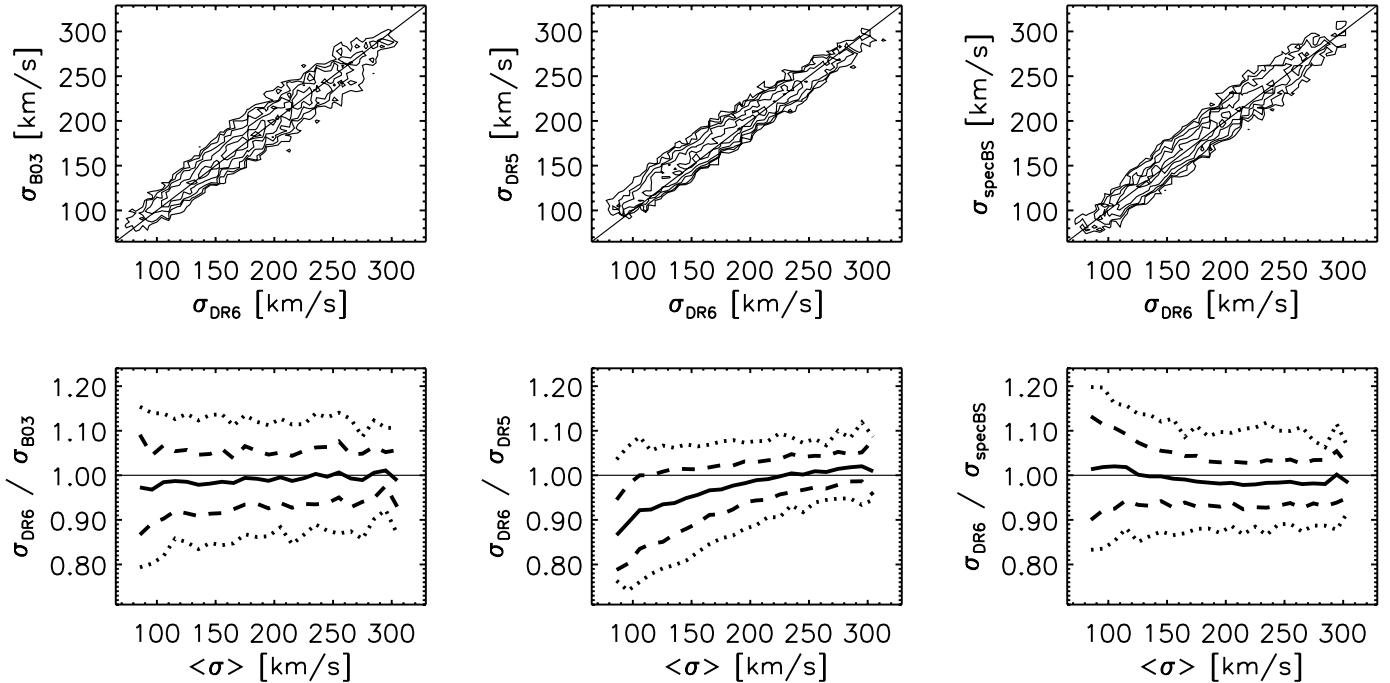
FIG. 8.—*Top*: Velocity dispersion measurements from B03 (*left*), DR5 (*middle*), and specBS (*right*) vs. the `spectro1d` DR6 values for the sample of elliptical galaxies used in Bernardi et al. (2003a). *Bottom*: Ratio of DR6 values to the other three samples (i.e., B03, DR5, and specBS) vs. the mean value [e.g., left panel $\langle \sigma \rangle = (\sigma_{DR6} + \sigma_{B03})/2$]. The median value at each value of $\langle \sigma \rangle$ is shown as a solid line; the values including 68% and 95% of the points are given as the dashed and dotted lines, respectively.

`Hammer` code are available for stars of type F0 and cooler in DR6.

Tests of the accuracy of the `Hammer` code with degraded (S/N $\sim$ 5) STELIB (Le Borgne et al. 2003), MILES (Sánchez-Blázquez et al. 2006), and SDSS (Hawley et al. 2002) dwarf template spectra reveal that the `Hammer` code assigns spectral types accurate to within ± 2 subtypes for K and M stars. The `Hammer` code can return results for warmer stars, but as the index set is optimized for cool stars, typical uncertainties are ± 4 subtypes for A–G stars at S/N $\sim$ 5; in this temperature regime, SSPP atmospheric parameters are a more reliable indicator of T_{eff}.

Given SEGUE's science goals, we emphasize two limitations to the accuracy of spectral types derived by the `Hammer` code.

1. The `Hammer` code uses spectral indices derived from dwarf standards; spectral types assigned to giant stars will likely have larger and systematic uncertainties.

2. The `Hammer` code was developed in the context of the SDSS high-latitude spectroscopic program; the use of broadband color ratios in the index set will likely make the spectral types estimated by the `Hammer` code particularly sensitive to reddening. Spectral types derived in areas of high extinction (i.e., low-latitude SEGUE plates) should be considered highly uncertain until verified with reddening-insensitive spectral indices.

4.4. *Correction of Biases in the Velocity Dispersions*

Both specBS and `spectro1d` measure velocity dispersions (σ) for galaxies; specBS does so, as described above, by including it as a term in the direct χ^2 fit of templates to galaxies. The velocity dispersion in `spectro1d` was computed as the average of the *Fourier*- and *direct-fitting* methods (Appendix B of Bernardi et al. 2003b, hereafter B03). However, because of changes in the spectroscopic reductions from the EDR to later releases, a bias appeared in the recent values available in the CAS. As shown

in Appendix A of Bernardi (2007), σ values in the DR5 do not match the values used by B03. The difference is small but systematic, with `spectro1d` DR5 larger than B03 at $\sigma \leq 150$ km s^{-1}. A similar bias is seen when comparing `spectro1d` DR5 with measurements from the literature (using the HyperLeda database; Paturel et al. 2003). Simulations similar to those in B03 show that the discrepancy results from the fact that the Fourier-fitting method is biased by $\sim$15% at low dispersions ($\sim$100 km s^{-1}), whereas the direct-fitting method is not. We therefore use only the direct-fitting method in DR6. Figure 8 shows comparisons of the `spectro1d` DR6 velocity dispersions with those from B03, DR5, and the specBS measurements. There is good agreement between `spectro1d` DR6 and B03 (rms scatter $\sim$7.5%), and between `spectro1d` DR6 and specBS (rms scatter $\sim$6.5%), whereas `spectro1d` DR5 is clearly biased high at $\sigma \leq 150$ km s^{-1}. The agreement between `spectro1d` DR6 and specBS is not surprising, since both are now based only on the direct-fitting method. The specBS measurements tend to be slightly smaller than DR6 at $\sigma \leq 100$ km s^{-1}; specBS is similarly smaller than HyperLeda, whereas DR6 agrees with HyperLeda at these low dispersions.

Figure 9 shows the distribution of the error on the measured velocity dispersions. The direct-fitting method used by `spectro1d` gives slightly larger errors than does the Fourier-fitting method, peaking at $\sim$10%. The figure shows that this error distribution is consistent with that found by comparing the velocity dispersions of $\sim$300 objects from DR2 which had been observed more than once.

Finally, HyperLeda reports substantially larger velocity dispersions than SDSS at $\sigma \geq 250$ km s^{-1}. The excellent agreement between three methods (direct fitting, cross-correlation, and Fourier-fitting) applied to the SDSS spectra at the high-velocity dispersion end gives us confidence in our velocity dispersions (Bernardi 2007), although it is unclear why the literature values are higher.
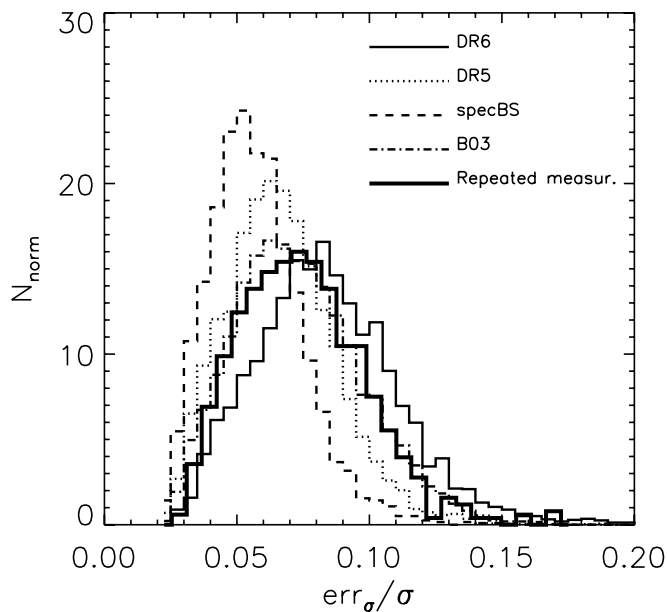
Fig. 9.—Error distribution of the velocity dispersion measurements from `spectro1d` DR6 (*thin solid line*), `spectro1d` DR5 (*dotted line*), specBS (*dashed line*), and B03 (*dot-dashed line*). The thick solid line was obtained by comparing the velocity dispersions of ~300 galaxies which had been observed two or more times; it is thus an empirical estimate of the true error. [*See the electronic edition of the Supplement for a color version of this figure.*]

4.5. *Linking SEGUE Imaging and Spectroscopy*

For the Legacy imaging, there exist simple links between the spectroscopic and imaging data, but these links are not yet in place between all the SEGUE spectroscopy and imaging. In particular, to obtain BEST or übercalibrated stellar photometry of SEGUE spectroscopic objects within CAS, one must perform an `SQL join` command between the spectroscopic SpecObjAll or sppParams tables in the CAS with the corresponding photometric tables (PhotoObjAll, SEGUEDR6.PhotoObjAll, or UberCal). Sample queries on how to do this are provided on the SDSS Web site. We plan to simplify this procedure in future data releases.

5. CONCLUSIONS AND THE FUTURE

We have presented the Sixth Data Release of the Sloan Digital Sky Survey. It includes 9583 deg^2 of imaging data, including a contiguous area of 7668 deg^2 of the northern Galactic cap. The data release includes almost 1.3 million spectra selected over 7425 deg^2 of sky, representing a 20% increment over the previous data release. This data release includes the first year of data from the SDSS-II, and thus includes extensive low-latitude imaging data, and a great deal of stellar spectroscopy. New to this data release are the following.

1. 1592 deg^2 of imaging data at lower Galactic latitudes, as part of the SEGUE survey, of which 1166 deg^2 are in searchable catalogs in the CAS.

2. Revised photometric calibration for the imaging data, with uncertainties of 1% in *g*, *r*, *i*, and *z*, and 2% in *u*.

3. Improved wavelength and flux calibration of spectra.

4. Detailed surface temperatures, metallicities, and gravities for stars.

The SDSS-II will end operations in the summer of 2008, at which point the Legacy project will have completed spectroscopy for the entire contiguous area of the northern cap region now covered by imaging, and SEGUE will have obtained spectra for 240,000 stars. The Supernova Survey (Frieman et al. 2007) has discovered 327 spectroscopically confirmed Type Ia supernovae to date in its first two seasons and has one more season to go.

REFERENCES

Abazajian, K., et al. 2003, AJ, 126, 2081 (DR1 paper)
———. 2004, AJ, 128, 502 (DR2 paper)
———. 2005, AJ, 129, 1755 (DR3 paper)
Adelman-McCarthy, J. K., et al. 2006, ApJS, 162, 38 (DR4 paper)
———. 2007, ApJS, 172, 634 (DR5 paper)
Allen, L. E., & Strom, K. M. 1995, AJ, 109, 1379
Allende Prieto, C., Beers, T. C., Wilhelm, R., Newberg, H. J., Rockosi, C. M., Yanny, B., & Lee, Y. S. 2006, ApJ, 636, 804
———. 2007, preprint (arXiv: 0710.5780)
Bagnulo, S., Jehin, E., Ledoux, C., Cabanac, R., Melo, C., Gilmozzi, R., & the ESO Paranal Science Operations Team. 2003, Messenger, 114, 10
Beers, T. C., Rossi, S., Norris, J. E., Ryan, S. G., & Shefler, T. 1999, AJ, 117, 981
Bernardi, M. 2007, AJ, 133, 1954
Bernardi, M., Hyde, J. B., Sheth, R. K., Miller, C. J., & Nichol, R. C. 2007, AJ, 133, 1741
Bernardi, M., et al. 2003a, AJ, 125, 1817
———. 2003b, AJ, 125, 1882 (B03)
Blanton, M. R., Eisenstein, D., Hogg, D. W., Schlegel, D. J., & Brinkmann, J, 2005a, ApJ, 629, 143

Blanton, M. R., Lin, H., Lupton, R. H., Maley, F. M., Young, N., Zehavi, I., & Loveday, J. 2003, AJ, 125, 2276
Blanton, M. R., et al. 2005b, AJ, 129, 2562
Castelli, F., & Kurucz, R. L. 2003, in Poster Papers, IAU Symp. 210, Modeling of Stellar Atmospheres, ed. N. Piskunov, W. W. Weiss, & D. F. Gray (San Francisco: ASP), A20
Cenarro, A. J., Gorgas, J., Cardiel, N., Pedraz, S., Peletier, R. F., & Vazdekis, A. 2001, MNRAS, 326, 981
Chiu, K., Fan, X., Leggett, S. K., Golimowski, D. A., Zheng, W., Geballe, T. R., Schneider, D. P., & Brinkmann, J. 2006, AJ, 131, 2722
Clewley, L., Warren, S. J., Hewett, P. C., Norris, J. E., & Evans, N. W. 2004, MNRAS, 352, 285
Collinge, M., et al. 2005, AJ, 129, 2542
Covey, K. R., et al. 2007, AJ, 134, 2398
da Costa, L. N., Bernardi, M., Alonso, M. V., Wegner, G., Willmer, C. N. A., Pellegrini, P. S., Rité, C., & Maia, M. A. G. 2000, AJ, 120, 95
Davenport, J. R. A., Bochanski, J. J., Covey, K. R., Hawley, S. L., & West, A. A. 2007, AJ, 134, 2430
de Vaucouleurs, G. 1948, Ann. d'Astrophys., 11, 247

Dufour, P., et al. 2007, ApJ, 663, 1291
Eisenstein, D. J., et al. 2001, AJ, 122, 2267
———. 2006, AJ, 132, 676
Finkbeiner, D. P., et al. 2004, AJ, 128, 2577
Frieman, J. A., et al. 2008, AJ, 135, 338
Fukugita, M., Ichikawa, T., Gunn, J. E., Doi, M., Shimasaku, K., & Schneider, D. P. 1996, AJ, 111, 1748
Gates, E., et al. 2004, ApJ, 612, L129
Glazebrook, K., Offer, A. R., & Deeley, K. 1998, ApJ, 492, 98
Gray, R. O., & Corbally, C. J. 1994, AJ, 107, 742
Gray, R. O., Graham, P. W., & Hoyt, S. R. 2001, AJ, 121, 2159
Gunn, J. E., et al. 1998, AJ, 116, 3040
———. 2006, AJ, 131, 2332
Hall, P. B., et al. 2002, ApJS, 141, 267
Harris, H. C., et al. 2006, AJ, 131, 571
Hawley, S. L., et al. 2002, AJ, 123, 3409
Helmi, A., et al. 2003, ApJ, 586, 195
Hewett, P. C., Irwin, M. J., Skillman, E. D., Foltz, C. B., Willis, J. P., Warren, S. J., & Walton, N. A. 2003, ApJ, 599, L37
Hogg, D. W., Finkbeiner, D. P., Schlegel, D. J., & Gunn, J. E. 2001, AJ, 122, 2129
Holberg, J. B., & Bergeron, P. 2006, AJ, 132, 1221
Ivezić, Ž. et al. 2004, Astron. Nachr., 325, 583
———. 2007, AJ, 134, 973
Johnston, D. E., et al. 2003, AJ, 126, 2281
Lauer, T. R., et al. 2007, ApJ, 662, 808
Le Borgne, J.-F., et al. 2003, A&A, 402, 433
Lee, Y. S., et al. 2007a, preprint (arXiv: 0710.5645)
———. 2007b, preprint (arXiv: 0710.5778)
Lenz, D., Newberg, H., Rosner, R., Richards, G. T., & Stoughton, C. 1998, ApJS, 119, 121
Lépine, S, Rich, R. M., Shara, M. M., Cruz, K. L., & Skemer, A. 2007, ApJ, 668, 507
Lépine, S., & Shara, M. M. 2005, AJ, 129, 1483
Lisker, T., Grebel, E. K., Binggeli, B., & Glatt, K. 2007, ApJ, 660, 1186
Lupton, R. H., Gunn, J. E., Ivezić, Ž., Knapp, G. R., & Kent, S. 2001, in ASP Conf. Ser. 238, Astronomical Data Analysis Software and Systems X, ed. F. R. Harnden, Jr., F. A. Primini, & H. E. Payne (San Francisco: ASP), 269

Lupton, R. H., Gunn, J. E., & Szalay, A. S. 1999, AJ, 118, 1406
Mandelbaum, R., et al. 2005, MNRAS, 361, 1287
McDonald, P., et al. 2006, ApJS, 163, 80
Miller, C. J., et al. 2005, AJ, 130, 968
Monet, D. G., et al. 2003, AJ, 125, 984
Morrison, H. L., Norris, J., Mateo, M., Shectman, S. A., Dohm-Palmer, R. C., Helmi, A., & Freeman, K. 2003, AJ, 125, 2502
Morrison, H. L., Olszewski, E. W., Mateo, M., Norris, J. E., Harding, P., Dohm-Palmer, R. C., & Freeman, K. C. 2001, AJ, 121, 283
Munn, J. A., et al. 2004, AJ, 127, 3034
Padmanabhan, N., et al. 2008, ApJ, 674, 1217
Paturel, G., Petit, C., Prugniel, P., Theureau, G., Rousseau, J., Brouty, M., Dubois, P., & Cambrésy, L. 2003, A&A, 412, 45
Pier, J. R., Munn, J. A., Hindsley, R. B., Hennessy, G. S., Kent, S. M., Lupton, R. H., & Ivezić, Ž. 2003, AJ, 125, 1559
Prugniel, P., & Soubiran, C. 2001, A&A, 369, 1048
Re Fiorentin, P., Bailer-Jones, C. A. L., Lee, Y. S., Beers, T. C., Sivarani, T., Wilhelm, R., Allende Prieto, C., & Norris, J. E. 2007, A&A, 467, 1373
Richards, G. T., et al. 2002, AJ, 123, 2945
Sánchez-Blázquez, P., et al. 2006, MNRAS, 371, 703
Schlegel, D.J, Finkbeiner, D. P., & Davis, M. 1998, ApJ, 500, 525 (SFD98)
Schmidt, G. D., et al. 2003, ApJ, 595, 1101
Schreiber, M. R., & Gänsicke, B. T. 2003, A&A, 406, 305
Sirko, E., et al. 2004, AJ, 127, 899
Smith, J. A., et al. 2002, AJ, 123, 2121
Stoughton, C., et al. 2002, AJ, 123, 485 (EDR paper)
Strauss, M. A., et al. 2002, AJ, 124, 1810
Subbarao, M., Frieman, J., Bernardi, M., Loveday, J., Nichol, B., Castander, F., & Meiksin, A. 2002, Proc. SPIE, 4847, 452
Tucker, D., et al. 2006, Astron. Nachr., 327, 821
Valdes, F., Gupta, R., Rose, J. A., Singh, H. P., & Bell, D. J. 2004, ApJS, 152, 251
Vanden Berk, D. E., et al. 2004, ApJ, 601, 692
Wilhite, B. C., Vanden Berk, D. E., Kron, R. G., Schneider, D. P., Pereyra, N., Brunner, R. J., Richards, G. T., & Brinkmann, J. V. 2005, ApJ, 633, 638
Woolf, V. M., & Wallerstein, G. W. 2006, PASP, 118, 218
York, D. G., et al. 2000, AJ, 120, 1579